The Astrophysical Journal, 834:133 (18pp), 2017 January 10 doi:10.3847/1538-4357/834/2/133

A COUPLED 2 × 2D BABCOCK–LEIGHTON SOLAR DYNAMO MODEL. II. REFERENCE DYNAMO SOLUTIONS

Alexandre Lemerle[1,2] and Paul Charbonneau[1]
[1] Département de physique, Université de Montréal, 2900 Boulevard Édouard-Montpetit, Montréal, QC, H3T 1J4, Canada; lemerle@astro.umontreal.ca, paulchar@astro.umontreal.ca
[2] Collège de Bois-de-Boulogne, 10555 Avenue Bois-de-Boulogne, Montréal, QC, H4N 1L4, Canada
Received 2016 April 12; revised 2016 October 30; accepted 2016 November 8; published 2017 January 9

ABSTRACT

In this paper we complete the presentation of a new hybrid 2 × 2D flux transport dynamo (FTD) model of the solar cycle based on the Babcock–Leighton mechanism of poloidal magnetic field regeneration via the surface decay of bipolar magnetic regions (BMRs). This hybrid model is constructed by allowing the surface flux transport (SFT) simulation described in Lemerle et al. to provide the poloidal source term to an axisymmetric FTD simulation defined in a meridional plane, which in turn generates the BMRs required by the SFT. A key aspect of this coupling is the definition of an emergence function describing the probability of BMR emergence as a function of the spatial distribution of the internal axisymmetric magnetic field. We use a genetic algorithm to calibrate this function, together with other model parameters, against observed cycle 21 emergence data. We present a reference dynamo solution reproducing many solar cycle characteristics, including good hemispheric coupling, phase relationship between the surface dipole and the BMR-generating internal field, and correlation between dipole strength at cycle maximum and peak amplitude of the next cycle. The saturation of the cycle amplitude takes place through the quenching of the BMR tilt as a function of the internal field. The observed statistical scatter about the mean BMR tilt, built into the model, acts as a source of stochasticity which dominates amplitude fluctuations. The model thus can produce Dalton-like epochs of strongly suppressed cycle amplitude lasting a few cycles and can even shut off entirely following an unfavorable sequence of emergence events.

Key words: dynamo – Sun: activity – Sun: interior – Sun: magnetic fields – Sun: photosphere – sunspots

1. INTRODUCTION

Close to a century has now gone by since the discovery of the underlying magnetic nature of the eleven-year sunspot cycle (Hale et al. 1919). The magnetic polarity reversals of the leading and following (with respect to rotation) components of large bipolar magnetic regions (BMRs) is now thought to reflect the presence, somewhere in the solar interior, of a large-scale, dominantly axisymmetric zonally oriented (toroidal) magnetic field, antisymmetric about the Sun's equator and itself undergoing polarity reversals approximately every eleven years, for a full magnetic cycle period of $\simeq$22 years. The rotational shear of a pre-existing dipole, later detected on the solar surface (Babcock & Babcock 1955), can act as an inductive source for such an internal toroidal magnetic flux system. However, closing the dynamo loop requires an inductive mechanism capable of regenerating the dipole from this internal toroidal component, in a manner such as to lead the cyclic polarity reversals of both of these large-scale components of the solar magnetic field.

Many candidates for this toroidal-to-poloidal hydromagnetic inductive mechanism have been identified, starting with cyclonic convection (Parker 1955) and its associated mean electromotive force, and the surface decay of BMRs (Babcock 1961), now referred to as the Babcock–Leighton (BL) mechanism. These were joined more recently by helical waves along thin magnetic flux tubes (Schmitt 1987; Ossendrijver 2000), and shear instabilities in the tachocline (Dikpati & Gilman 2001), the stably stratified rotational shear layer located beneath the base of the solar convection zone, as revealed by helioseismology. In all cases, the rotational influence mediated by the Coriolis force is the key agent that breaks the mirror symmetry of the inductive flows, thus allowing one to circumvent Cowling's theorem.

Of these various candidates for poloidal field regeneration, the BL mechanism stands out as the only one that can be directly observed operating at the solar surface, and as such is far better constrained than any other. In particular, the distribution of tilt angles of BMRs, namely the angle defined by a line segment joining each pole of the BMR measured with respect to the east–west direction, is now well characterized from white light (Howard 1991; Dasi-Espuig et al. 2010) and magnetographic observations (Wang & Sheeley 1989). This tilt arises through the action of the Coriolis force, and associated with it is a net dipole moment so that, effectively, a poloidal magnetic component is being produced from the pre-existing deep-seated toroidal component, ultimately giving rise to emerging BMRs (see Fan 2009 for a review). The magnitude of this tilt, and its pattern of variations with latitude, BMR flux and separation, and statistical fluctuations about the mean, all play a key role in setting the magnitude of the surface dipole moment produced in the course of a sunspot cycle.

Because the BL mechanism operates at the solar surface, a transport mechanism is also needed to carry the surface poloidal magnetic field down into the interior, where rotational shearing is taking place. Here again a number of appropriate candidate mechanisms are available, including advection by large-scale meridional flows pervading the solar convection zone, as well as turbulent transport effects, namely isotropic diffusive transport and directional turbulent pumping. Viewed globally, the BL mechanism is a non-local inductive effect: the surface source of poloidal field is driven by the deep-seated toroidal component, on timescales much shorter than the magnetic cycle period.

Dynamo models of the solar cycle relying on the BL mechanism of poloidal field regeneration have undergone a vigorous revival in the last 25 years or so, spurred by Wang et al. (1989), Wang & Sheeley (1991), Choudhuri et al. (1995), and Durney (1995). Many such models are now dispersed in the literature (for recent reviews see Charbonneau 2010; Karak et al. 2014). The vast majority rely on a two-dimensional axisymmetric formulation of the problem, whereby the large-scale flows and magnetic field components are both axisymmetric, and the dynamo equations solved in a meridional (r, θ) plane. Typically, helioseismology-compatible parameterizations for solar-like internal differential rotation and meridional circulation are introduced, and these flows are assumed steady (the so-called kinematic approximation).

Many such models do differ in how they incorporate the BL mechanism, a fundamentally non-axisymmetric effect, into the axisymmetric dynamo equations (compare, e.g., Durney 1995; Dikpati & Charbonneau 1999; Nandy & Choudhuri 2001; Muñoz-Jaramillo et al. 2010). They also differ in assumptions made regarding the primary magnetic field transport mechanism. As a consequence, models based on rather different input physics can do roughly as well as one another in reproducing the primary characteristics of the observed solar cycle. However, the differences can matter a lot in practice. Perhaps no better illustration of this point can be found than the widely differing dynamo model-based predictions of sunspot cycle 24 made by Dikpati et al. (2006) and Choudhuri et al. (2007), each using a distinct BL model "calibrated" to earlier sunspot cycles.

This problem is compounded when introducing data assimilation into the model-based prediction, as the data sets must then also be preprocessed in some way to accommodate the axisymmetric formulation of the dynamo model used for forecasting. Both the afore-cited model-based prediction schemes used distinct geometrically simplified implementations of different data sets being assimilated, and in all likelihood these differences also contributed to the widely varying predictions for the amplitude of cycle 24. Ideally, data assimilation should be carried out using full-disk magnetograms and/or detailed observations of active region emergences, including complete positional and timing information. Either way, this requires a dynamo model with a geometrically complete representation of the solar surface, and thus demands abandoning axisymmetry.

One extreme possibility consists in turning to global magnetohydrodynamical (MHD) simulations of solar convection. Despite remarkable progress in the past decade (for a review see, e.g., Section 3 of Charbonneau 2014), such simulations still cannot accommodate sufficient spatial resolution to resolve convection and magnetic field evolution in the surface layers, or even capture the interior process of magnetic flux rope formation and buoyant rise (but on the latter see Nelson et al. 2013, 2014; Fan & Fang 2014). Typically, such simulations also fail to drive regular, solar-like polarity cyclic reversals in the large-scale magnetic field they generate (but see Passos & Charbonneau 2014 for the closest results yet).

Intermediate approaches are also possible: finding a way to include the full non-axisymmetric representation of, at least, the surface processes, while retaining the kinematic approach for the transport of magnetic flux. To our knowledge, only two such models exist in the literature (Yeates & Muñoz-Jaramillo 2013; Miesch & Dikpati 2014, hereafter MD2014), as they include a full three-dimensional kinematic representation of the solar convection zone up to the surface. Here again, they mostly differ in how they incorporate the localized emergence of new magnetic flux: Yeates & Muñoz-Jaramillo (2013) impose localized flow perturbations at the base of the convection zone to trigger the eruption of active regions out of the toroidal flux, while MD2014 and Miesch & Teweldebirhan (2015) apply a surface flux deposition technique, through an empirical masking of the deep-seated toroidal field.

In this series of papers we present a BL dynamo model that belongs to this same category. We retain a fairly conventional two-dimensional axisymmetric kinematic flux transport dynamo (FTD) model, specifically the model described in Charbonneau et al. (2005), without its non-local poloidal source term, and couple it to a two-dimensional surface flux transport (SFT) simulation. The latter provides the source term for the former through the upper boundary condition, and in turn the FTD provides the emergences required as input to the SFT simulation. We opted to call this a "2×2D" dynamo model. This is still a kinematic model, in that it uses steady parametrized large-scale flow fields compatible with helioseismology and surface measurements. Specifying the form of these flows requires the adjustment of many model parameters, in order to generate the most "solar-like" dynamo solutions possible.

In Lemerle et al. (2015, hereafter Paper I) we introduced a genetic algorithm-based method for formally carrying out this optimization problem, in the context of the SFT simulation. The optimization process is set to minimize deviations with respect to synoptic magnetograms (and derived global quantities). Not only does this approach find an optimal solution, but it also allows us to map a range of acceptable solutions, thus providing robust Monte Carlo-like confidence intervals on best-fit model parameters and allowing the identification of parameter degeneracies. A key result is that the range of acceptable surface meridional flow profiles nicely fits surface Doppler measurements (Ulrich 2010), even though these data are not used to constrain the optimization process.

In the present paper we extend the procedure to the coupled model described above, and thus produce an "optimal" 2×2D BL dynamo model of the solar cycle. The use of quotes is motivated by the fact that even this basic optimal model involves unavoidable stochastic components, associated with the flux emergence process, so that it can only fit the Sun (meaning, e.g., the sunspot number (SSN) time series) in a statistical sense. Indeed, the SFT solutions presented in Paper I already show how the uncertainties in global cycle characteristics are dominated by the inherent stochasticity of the flux emergence process.

In Section 2 we discuss the formulation of the coupled model and its components. In Section 3 we turn to its calibration against observed solar features. In Section 4 we present self-consistent reference dynamo solutions and examine their patterns of long term variability. In Section 5 we discuss the limitations of the calibration technique and compare some of the results with direct solar observations. We conclude by summarizing our most salient results as well as possible paths of improvement and ongoing work.

2. MODEL

The contemporary version of the original scenario proposed by Babcock (1959) runs as follows:

(0) at solar maximum, strong toroidal magnetic fields are present deep in the solar interior, antisymmetric with respect to the equator;
(i) during the ascending and descending phases of the solar cycle, toroidal flux loops rise and emerge at the solar surface in the form of BMRs, twisted due to the Coriolis effect, such that the western spots tend to be closer to the equator (tilt following on average Joy's law);
(ii) surface diffusion/transport near the equator allows for more cancellation of the western polarities, when merging with their counterparts from the other hemisphere, leaving the remaining "eastern" flux to be transported toward the poles and trigger the polarity reversal of magnetic polar caps;
(iii) the new surface dipole is subducted and sheared by differential rotation, building up a new internal toroidal magnetic structure, opposite to the preceding one and ready for...
(iv) ...the generation of a new population of BMRs during the next half-cycle (from now on, we refer to this half magnetic cycle, or sunspot cycle, as simply a "cycle").

The numerical implementation we propose for carrying out this scheme is quite simple:

(i) new BMRs are continuously deposited at the solar surface, at times, latitudes and longitudes, tilts, angular separations, magnetic fluxes and polarity generated through a (probabilistic) flux emergence algorithm based on the strength and spatial distribution of the deep-seated magnetic fields;
(ii) the SFT equation is solved on the solar spherical surface, and generates the expected cancellation, decay, transport and specific features typically observed in surface magnetograms (see Paper I);
(iii) the FTD equation is solved in the meridional plane, using the evolving results of the surface simulation as a time-dependent upper boundary condition on the poloidal field; transport of this poloidal field to the base of the convection zone and subsequent shearing by differential rotation eventually builds up strong toroidal magnetic fields deep in the convection zone;
(iv) the dynamo loop is closed by allowing this deep-seated magnetic structure to generate the emergences required in step (i).

2.1. Basic Ingredients

In the depths of the solar convection zone or in the tangles of photospheric turbulent motions, magnetic fields are dispersed, transported, amplified or destroyed by small and large-scale flows. In the solar interior and photosphere, these processes are well-captured by the MHD induction equation:

$$\frac{\partial \boldsymbol{B}}{\partial t} = \boldsymbol{\nabla} \times (\boldsymbol{u} \times \boldsymbol{B} - \eta \boldsymbol{\nabla} \times \boldsymbol{B}), \tag{1}$$

with η the net magnetic diffusivity, including contributions from the small microscopic magnetic diffusivity $\eta_e = c^2/4\pi\sigma_e$ (with σ_e^{-1} the electric resistivity of the plasma), as well as a dominant turbulent contribution associated with the destructive folding of magnetic field lines by small-scale convective fluid motions. We adopt here the kinematic approximation, whereby the flow $\boldsymbol{u}$ is considered given. This approximation has been shown to be appropriate in reproducing reasonably well the synoptic evolution of the solar surface magnetic field (see, e.g., Wang et al. 2002a; Baumann et al. 2004), as well as the overall solar dynamo properties (see, e.g., Karak et al. 2014, and references therein). On spatial scales much larger than convection, two flows contribute to $\boldsymbol{u}$: meridional circulation $\boldsymbol{u}_{\rm P}(r, \theta)$ and differential rotation $\varpi\Omega(r, \theta)\hat{\boldsymbol{e}}_\phi$. Both these flows can be considered axisymmetric ($\partial/\partial\phi \equiv 0$) and steady ($\partial/\partial t \equiv 0$) as per the kinematic approximation. They can be expressed in spherical polar coordinates (r, θ, ϕ) as

$$\boldsymbol{u}(r, \theta) = \underbrace{\frac{R}{\rho(r)/\rho_0}\boldsymbol{\nabla} \times (\Psi(r, \theta)\hat{\boldsymbol{e}}_\phi)}_{\boldsymbol{u}_{\rm P}(r,\theta)=u_r(r,\theta)\hat{\boldsymbol{e}}_r+u_\theta(r,\theta)\hat{\boldsymbol{e}}_\theta} + \varpi\Omega(r, \theta)\hat{\boldsymbol{e}}_\phi, \tag{2}$$

where the meridional flow has been formulated in terms of a stream function $\Psi(r, \theta)$, thus ensuring mass conservation in a $\rho(r) = \rho_0\xi^m$ density profile, with $\xi(r) = (R/r) - 1$, $m = 1.5$ for an adiabatic stratification, R the solar radius, and $\varpi = r\sin\theta$.

2.1.1. Meridional Circulation

We opted to use a modified form of the meridional flow profile introduced by van Ballegooijen & Choudhuri (1988). This flow can be defined through a separable stream function of the form:

$$\Psi(r, \theta) = u_\theta(R, \theta)\frac{R}{r}\left[-\frac{\xi^{m+1}}{m+1} + \frac{c_1\xi^{2m+1}}{2m+1} - \frac{c_2\xi^{2m+p+1}}{2m+p+1}\right], \tag{3a}$$

where

$$c_1 = \frac{(2m+1)(m+p)}{(m+1)p}\xi_b^{-m},$$
$$c_2 = \frac{(2m+p+1)m}{(m+1)p}\xi_b^{-(m+p)},$$

and $\xi_b = (R/R_b) - 1$. Parameters p and m determine the depth and concentration of the return flow, down to $r = R_b$. For the purpose of the foregoing analysis and calibration, parameters p and R_b will be treated as free parameters, while the polytropic index m is set at 1.5, appropriate for an adiabatic stratification.

We deviate from the original formulation of van Ballegooijen & Choudhuri (1988) by using the following latitudinal dependence, also used in Paper I:

$$u_\theta(R, \theta) = -\frac{u_0}{u_0^*}\,\mathrm{erf}^q(v\sin\theta)\,\mathrm{erf}^n(w\cos\theta), \tag{3b}$$

with u_0^* a normalization factor such that u_0 is the maximum meridional flow velocity and q, n, v, and w parameters that allow us to generate a very wide range of solar-like surface meridional flow profiles. The value of n is fixed to 1 as to prevent the formation of a $0\,\mathrm{m\,s^{-1}}$ plateau near the equator. We developed this flexible formulation in Paper I to allow for the inclusion of various profiles used in flux transport modeling (e.g., van Ballegooijen & Choudhuri 1988; Dikpati & Charbonneau 1999; Wang et al. 2002b) and measured on the Sun (e.g., Ulrich 2010).

2.1.2. Differential Rotation

Unlike meridional circulation, the solar internal differential rotation profile is well constrained by helioseismology. We use here the helioseismically calibrated solar-like parameterization introduced in Charbonneau et al. (1999):

$$\Omega(r,\,\theta) = \Omega_c + \frac{\Omega(R,\,\theta) - \Omega_c}{2}\left[1 + \mathrm{erf}\left(\frac{r - R_c}{\delta_c/2}\right)\right], \quad (4a)$$

with $\Omega_c = 2.724\ \mu\mathrm{rad\ s}^{-1}$, $R_c = 0.7R$, and surface rotation

$$\Omega(R,\,\theta) = \Omega_0(1 + a_2\cos^2\theta + a_4\cos^4\theta), \quad (4b)$$

where $a_2 = -0.1264$, $a_4 = -0.1591$, and $\Omega_0 = 2.894\ \mu\mathrm{rad\ s}^{-1}$ (see also Snodgrass 1983). The thickness δ_c of the transition region between differential and solid rotation, the tachocline, near the base of the convection zone, is kept as a free parameter.

2.1.3. Magnetic Diffusivity

In the stably stratified core, the presumed absence of turbulence suggests a net diffusivity (η_c) given by Ohmic dissipation, while in the bulk of the convection zone, enhanced turbulent dissipation (η_t) of the magnetic field is expected to dominate. The following parametric profile, given by Dikpati & Charbonneau (1999), allows for a smooth transition between these two regimes:

$$\eta(r) = \eta_c + \frac{\eta_t}{2}\left[1 + \mathrm{erf}\left(\frac{r - R_c}{\delta_c/2}\right)\right], \quad (5)$$

where R_c takes the same value as in the preceding differential rotation profile.

In the surface layer, supergranular convective motions drive a random walk that disperses magnetic flux, and can be modeled as a diffusive process (Leighton 1964) characterized by an effective magnetic diffusivity of order $\eta_R \simeq 10^{12}$–$10^{13}\ \mathrm{cm^2\ s^{-1}}$. This value is used solely in the SFT part of the model. The overall radial profile of $\eta(r)$ consequently includes an implicit step function at $r = R$. The exact values for η_c, η_t, and η_R, as well as δ_c, are virtually impossible to determine from first principles, such that they must be treated as unknown parameters needing a proper calibration.

2.2. Flux Transport Dynamo

The large-scale axisymmetric magnetic field simulated in the FTD component of the model can be expressed as

$$\boldsymbol{B}(r,\,\theta,\,t) = \underbrace{\boldsymbol{\nabla}\times(A_\phi(r,\,\theta,\,t)\hat{\boldsymbol{e}}_\phi)}_{\boldsymbol{B}_\mathrm{P} = B_r\hat{\boldsymbol{e}}_r + B_\theta\hat{\boldsymbol{e}}_\theta} + B_\phi(r,\,\theta,\,t)\hat{\boldsymbol{e}}_\phi, \quad (6)$$

where $\boldsymbol{B}_\mathrm{P}$ and $B_\phi\hat{\boldsymbol{e}}_\phi$ are respectively the poloidal and toroidal vector components of the field. Inserting this decomposition for $\boldsymbol{B}$, along with Equation (2) for the flow, into the MHD induction Equation (1) then yields the usual two evolutionary equations for the scalar components $A_\phi(r,\,\theta,\,t)$ and $B_\phi(r,\,\theta,\,t)$:

$$\frac{\partial A_\phi}{\partial t} = -\frac{1}{\varpi}(\boldsymbol{u}_\mathrm{P}\cdot\boldsymbol{\nabla})(\varpi A_\phi) + \eta\left(\nabla^2 - \frac{1}{\varpi^2}\right)A_\phi, \quad (7a)$$

$$\frac{\partial B_\phi}{\partial t} = -\varpi(\boldsymbol{u}_\mathrm{P}\cdot\boldsymbol{\nabla})\left(\frac{B_\phi}{\varpi}\right) + \eta\left(\nabla^2 - \frac{1}{\varpi^2}\right)B_\phi - (\boldsymbol{\nabla}\cdot\boldsymbol{u}_\mathrm{P})B_\phi + \frac{1}{\varpi}\frac{\partial\eta}{\partial r}\frac{\partial(\varpi B_\phi)}{\partial r} + \varpi\boldsymbol{B}_\mathrm{P}\cdot\boldsymbol{\nabla}\Omega. \quad (7b)$$

These two equations are linear in A_ϕ and B_ϕ, but are coupled by the shearing term in Equation 7(b) which acts as a source for B_ϕ proportional to A_ϕ. No such source appears explicitly in Equation 7(a). Here the regeneration and amplification of the poloidal field is supplied by a continuous input from the SFT simulation, providing a time-evolving surface boundary condition for A_ϕ which effectively acts as a source.

2.3. Surface Flux Transport

Following earlier modeling work on surface magnetic flux evolution, in particular in Paper I, we consider the magnetic field to be predominantly radial on global scales and we solve only the r-component of Equation (1), at $r = R$. This leads to the usual two-dimensional linear advection–diffusion equation for the scalar component $B_R = B_r(R,\,\theta,\,\phi,\,t)$,

$$\frac{\partial B_R}{\partial t} = -\frac{1}{R\sin\theta}\frac{\partial}{\partial\theta}[u_\theta(R,\,\theta)B_R\sin\theta] - \Omega(R,\,\theta)\frac{\partial B_R}{\partial\phi} + \frac{\eta_R}{R^2}\left[\frac{1}{\sin\theta}\frac{\partial}{\partial\theta}\left(\sin\theta\frac{\partial B_R}{\partial\theta}\right) + \frac{1}{\sin^2\theta}\frac{\partial^2 B_R}{\partial\phi^2}\right] - \frac{B_R}{\tau_R} + S_\mathrm{BMR}(\theta,\,\phi,\,t), \quad (8)$$

to which two supplementary terms have been added: a source term $S_\mathrm{BMR}(\theta,\,\phi,\,t)$ to account for the discrete emergence of new surface flux in the form of BMRs, and a linear sink term $-B_R/\tau_R$ to allow for an exponential decay of the surface field with time. Schrijver et al. (2002) originally found such a decay on a timescale of 5–10 years to be necessary to preclude secular drift and ensure polarity reversal of the polar caps when modeling surface flux evolution over many successive cycles of differing amplitudes. This was subsequently justified physically by Baumann et al. (2006) as the effect of a vertical turbulent diffusion, or equivalently a convective submergence, on the decay of the dominant dipole mode, two physical mechanisms that cannot be directly included in the SFT model. We included this term in Paper I but did not find it to be required for the SFT results to match the synoptic magnetogram of cycle 21. We test it again here, with τ_R treated as a free parameter.

2.4. Numerical Solution and Coupling

The FTD Equations (7) and SFT Equation (8) are solved concurrently, each on a separate two-dimensional computational grid on which spatial discretization is carried out via the Galerkin finite-element method, and implicit temporal discretization through the one-step Θ-method (see, e.g., Burnett 1987).

The SFT simulation is solved over a regular Cartesian grid in $(\theta,\,\phi)$ representing the whole solar surface, with longitudinal periodicity enforced through a padding of ghost cells. Rigorous flux conservation is also required since only a small fraction of the emerging magnetic flux ultimately builds up the axial dipole observed at sunspot minima. We minimize numerical

discretization errors by adopting double precision arithmetics, a 256×128 longitude–latitude grid, and 8000 time steps for the eight-cycle runs that will be analyzed in Section 3 (for more details on numerical errors see Paper I, Section 2.4 and discussion therein).

The FTD simulation is solved simultaneously over a regular 96×128 Cartesian grid in (r, θ), from pole to pole and $0.5 \leqslant r/R \leqslant 3.0$. Below $r = 0.5R$, the radiative core is considered perfectly conductive and the $A_\phi = B_\phi = 0$ boundary condition is applied. For $r > R$, the absence of flows and electrical currents imposes $B_\phi = 0$. The spherical geometry finally constrains $A_\phi = B_\phi = 0$ at the poles. The overall scheme is similar to that described in Charbonneau et al. (2005).

With such spatial resolutions and typical time steps of $\simeq$4 and $\simeq$40 days respectively in the SFT and FTD simulations, the former dominates the computational workload by a factor of $\simeq$20.

2.4.1. From SFT to FTD

The surface ($r = R$) boundary condition on A_ϕ is updated at every FTD time step, via the longitudinal averaging of the SFT solution ($\langle B_R \rangle^\phi(\theta, t)$) and integration of the resulting latitudinal function:

$$A_\phi(R, \theta, t) = A_\phi^0 + \frac{R}{\sin\theta} \int \langle B_R \rangle^\phi(\theta, t) \sin\theta d\theta, \qquad (9)$$

where A_ϕ^0 is set to zero at the poles. This provides the coupling from the SFT toward the FTD model.

Such coupling assumes that physical processes responsible for surface magnetic flux evolution occur only inside the single FTD grid layer located at $r = R$, which is of thickness $\simeq$3.7 Mm for our working spatial mesh.

2.4.2. From FTD to SFT: Emergence Function

The coupling from the FTD toward the SFT is the emergence of BMRs. In view of the considerable complexity of the various processes involved in the formation, destabilization, buoyant rise, and emergence of deep-seated magnetic flux tubes (see, e.g., Weber et al. 2011 and review by Fan 2009), we opted here to input emerging BMRs directly into the SFT component of the model, based on a semi-empirical emergence function giving, as a function of the strength of the internal magnetic field, the *probability* that the emergence of a BMR will occur.

Calculations of the destabilization and buoyant rise of magnetic flux tubes carried out in the thin-tube approximation do offer some useful guidance. From the stability diagrams obtained by Schüssler et al. (1994) and Ferriz-Mas et al. (1994), one can infer the depth, latitude, and magnetic amplitudes at which toroidal flux tubes are expected to destabilize. According to their results, and depending on the level of subadiabaticity in the outer reaches of the radiative core, instability growth rates near $r/R \simeq 0.7$ remain approximately constant, or show a smooth increase with latitude, from the equator up to $\simeq$70°, and then fall off rapidly to zero over a latitudinal width of $\simeq$5°. A lower threshold of order 10^4–10^5 G is also required, on the amplitude of the magnetic field inside concentrated flux tubes. A crucial missing link is the degree of magnetic field amplification taking place during the formation of these toroidal flux tubes from the dynamo-generated large-scale magnetic field. Accordingly, we define this lower limit as $B^* \in [10^1, 10^4]$ (with units that depend on the exact parameterization of Equation (10) below), and treat it as another free parameter to be calibrated. Modeling also shows that a certain level of twist is required for the tube to maintain its coherence during the rise through the convective envelope (Fan 2009). Accordingly, we introduce the quantity $|B_{\rm mix}| = |B_\phi|^b |A_\phi|^a$, evaluated at depth $r^*/R \in [0.60, 0.80]$ and with exponents in the ranges $b \in [0.5, 3.0]$ and $a \in [0.0, 2.0]$, and use it to build the following quasi-normalized emergence function:

$$|F_B(\theta, t)| = \frac{1}{4}\left(1 + \mathrm{erf}\left(\frac{|B_{\rm mix}| - B^*}{\delta B^*}\right)\right) \left| \frac{B_{\rm mix}}{\max|B_{\rm mix}|} \right|^c \times \left((1 - \mu_\ell)\frac{|\ell|}{90} + \mu_\ell\right)\left(1 - \mathrm{erf}\left(\frac{|\ell| - \ell^*}{\delta\ell^*}\right)\right). \qquad (10)$$

The first part of Equation (10) sets a lower threshold on $B_{\rm mix}$ above which emergences can take place, as well as a possible saturation ($c \to 0$) or linear growth ($c \to 1$) of the probability above B^*. The transition scale δB^* is set to some fraction of B^* (see Section 3). The second part accounts for the latitudinal dependence of the instability's growth rate, which we assume to increase linearly from $\mu_\ell \in [0, 1]$ at the equator to 1 near latitude $\ell^* \in [65°, 90°]$, followed by a quick drop to zero in $\delta\ell^* = 3°$ (see Figures 1 and 2 of Ferriz-Mas et al. 1994). The sign of $F_B(\theta, t)$ is given by the sign of the input B_ϕ.

The emergence process is made inherently non-deterministic with the following sources of stochasticity:

(i) at every SFT time step, the number $N(t)$ of new BMRs to emerge is extracted from a uniform random distribution, proportional to the sum $\sum_\theta F_B(\theta, t)$ at the corresponding FTD time step;
(ii) the probability of emergence of a BMR at a given latitude is made proportional to $F_B(\theta, t)$.

Also, independently from the distribution of $F_B(\theta, t)$, and as determined in our analysis of Wang & Sheeley's (1989) database entries (see Appendix A of Paper I):

(iii) emergence longitudes are assumed to be random;
(iv) magnetic fluxes Φ are extracted from a log-normal distribution centered at $\log\Phi_0 = 21.3(\log Mx)$ with standard deviation $\sigma_{\log\Phi} = 0.5(\log Mx)$ (Paper I, Equation (13)), independently of cycle phase and amplitude (following Bogdan et al. 1988);
(v) magnetic bipole separations δ follow a power law with flux, with a Gaussian dispersion about it (Paper I, Equation (15));
(vi) magnetic bipole tilts α relative to the equatorial direction follow a linear increase with latitude (Joy's law) and a Gaussian spread with standard deviation decreasing exponentially with $\log\Phi$ (Paper I, Equations 16(a) and 16(b).

The input of BMRs in the SFT simulation enters the source term

$$S_{\rm BMR}(\theta, \phi, t) = \sum_{i=1}^{N(t)} B_i(\theta, \phi)\delta_D(t - t_i), \qquad (11a)$$

with δ_D the Dirac delta. Each new BMRs is placed at its given position (θ_i, ϕ_i) and time t_i, with a Gaussian distribution for each pole:

$$B_i(\theta, \phi) = \underbrace{B_{i0} e^{-\delta_{i+}^2/2\sigma^2}}_{B_{i+}(\theta,\phi)} + \underbrace{-B_{i0} e^{-\delta_{i-}^2/2\sigma^2}}_{B_{i-}(\theta,\phi)}, \quad (11b)$$

where δ_{i+} and δ_{i-} are the heliocentric angular distances from the centers (θ_{i+}, ϕ_{i+}) and (θ_{i-}, ϕ_{i-}) of the two poles, respectively, and $\sigma = 4°$ the width of the Gaussians.

The preceding steps dictate the relative probability of given emergences to occur, but the actual number $N(t)$ of BMRs to emerge every time step remains adjustable. We introduce a proportionality factor K between the emergence function $F_B(\theta, t)$ and the actual emerged butterfly diagram, so that $N(t) = K \cdot \sum_\theta F_B(\theta, t)$. Therefore, K effectively acts as a dynamo number in the model. Here however, the fact that the poloidal source term depends on a *number* of emergences $N(t)$, rather than being directly proportional to the underlying toroidal flux, means that the relationship is not formally linear. Nonetheless, as described in Section 4.1, the model appears to behave linearly when averaged over many different stochastic realizations of emergences. Stochastic aspects notwithstanding, K may thus be considered a dynamo number in a statistical sense, as it sets the mean growth rate in the linear regime. This dynamo number is akin to that encountered in the classical mean-field framework, where it is defined as the dimensionless product of the strength of differential rotation and turbulent electromotive force over magnetic dissipation. Moreover, as demonstrated by the dynamo solutions to be discussed presently, the value of K also sets the absolute mean amplitude of the dynamo, together with the tilt-quenching mechanism introduced in Section 4.2.

As a result, for the reference dynamo solution presented in Section 4.2, with the working spatial mesh and time stepping described above and after adjustment of K to obtain stable, solar-like solutions, the value of $N(t)$ varies from 5–15 per SFT time step (50–150 per month) near cycle maxima down to 0–1 per SFT time step (0–10 per month) at cycle minima.

Meanwhile, the exact distribution of these newly emerged BMRs, i.e., the shape of $F_B(\theta, t)$, is mostly critical if one strives to match the observed butterfly diagram. The next logical step is now to carry out a calibration of all parameters describing the full model, using observed emergences as a constraint, as detailed in the following section.

3. MODEL CALIBRATION

The various physical components of the coupled SFT–FTD model introduced in the preceding section jointly involve a large number of numerical parameters; 27 to be precise. Nine of these can be fixed confidently either through observations or theoretical considerations. Five (R_c, Ω_0, Ω_c, a_2, and a_4) are the numerical parameters defining the differential rotation profile (see Section 2.1.2), another (m) is the polytropic index characterizing the stratification within the convection zone, and yet another (n) is used to formulate a flexible surface meridional flow profile but is set to 1 to reflect solar observations (see Section 2.1.1). The last two parameters to be held fixed, δB^* and $\delta \ell^*$, control the shapes of the latitudinal and magnetic masking used in the emergence function (see Section 2.4.2); experimenting with the model reveals that within reasonably wide ranges, the exact values chosen for these parameters have little impact on the global dynamo behavior. Consequently, they are fixed at values $0.1B^*$ and 3° respectively.

This leaves 18 adjustable parameters, which are listed in Table 1. Eleven pertain to the linear terms in the model, including the shape of the meridional flow, magnetic diffusivity and surface sink (δ_c, R_b, u_0, p, q, v, w, η_c, η_t, η_R, and τ_R), and the remaining seven (r^*, b, a, c, B^*, ℓ^*, and μ_ℓ) to the form of the nonlinear emergence function (Equation (10)).

Table 1
Parameter Values

Parameters	[a]Reference Values ($C = 0.42$)	Tested Intervals	[b]Optimal Values ($C \in [0.92, 0.94]$)
r^*/R	0.705	[0.60, 0.80]	$\mathbf{0.68}\ ^{0.04}_{0.03}$
b	1.0	[0.5, 3.0]	$\mathbf{1.5}\ ^{1.5}_{0.5}$
a	0.0	[0.0, 2.0]	$\mathbf{0.0}\ ^{0.8}_{0.0}$
c	1.0	[0.0, 1.0]	$\mathbf{1.0}\ ^{0.0}_{0.6}$
B^* [c]	[d] 10^2	$[10^1, 10^4]$	$^2\mathbf{10}\ ^{0}_{10^2}$
ℓ^*	45	[64, 90]	$\mathbf{70}\ ^{9}_{6}$
μ_ℓ	0.0	[0.0, 1.0]	$\mathbf{0.5}\ ^{0.5}_{0.5}$
δ_c/R	0.05	[0.04, 0.10]	$\mathbf{0.05}\ ^{0.02}_{0.01}$
R_b/R	0.69	[0.60, 0.70]	$\mathbf{0.60}\ ^{0.02}_{0.00}$
u_0/ m s^{-1}	18	[e] [8, 18]	$\mathbf{17}\ ^{1}_{8}$
$\log p$	2.0	$[-1.0, 2.0]$	$\mathbf{-0.7}\ ^{1.2}_{0.2}$
q	2.5	[f] $[2^0, 2^5]$	$\mathbf{1}\ ^{31}_{0}$
v	1.0	[f] $[2^0, 2^3]$	$\mathbf{7}\ ^{1}_{5}$
w	3.5	[f] $[2^0, 2^5]$	$\mathbf{1}\ ^{1}_{0}$
$\log(\eta_c/\text{cm}^2\ \text{s}^{-1})$	9	[7, 11]	$\mathbf{8.0}\ ^{2.4}_{1.0}$
$\log(\eta_t/\text{cm}^2\ \text{s}^{-1})$	10.7	[11.0, 13.0]	$\mathbf{12.0}\ ^{0.2}_{0.4}$
$\log(\eta_R/\text{cm}^2\ \text{s}^{-1})$	12.48	[e] [12.38, 12.82]	$\mathbf{12.78}\ ^{0.04}_{0.40}$
τ_R/years	[g] 32	[e] [7, 32]	$\mathbf{10}\ ^{\infty}_{3}$

Notes.
[a] Reference values as to approximate velocity and diffusivity profiles and emergence algorithm used by MD2014, leading to the solution shown in Figure 1(a).
[b] Solutions for the first seven parameters (r^*, b, a, c, B^*, ℓ^*, and μ_ℓ) result from the full W21 × 8–18 optimization. Solutions for the remaining eleven parameters (δ_c, R_b, u_0, p, q, v, w, η_c, η_t, η_R, and τ_R) result from the subsequent W21 × 8–11 optimization. "Optimal values" listed in bold font correspond to one chosen optimal solution (see Figures 1(e) and (f)) among the acceptable solutions bounded by the given error bars. Other combinations of parameters allowed by the error bars should still be used with care, considering the shape of the parameter-space landscape inside the optimal region and in particular the correlations described at the end of Section 3.5.
[c] The units of B^* depend on the values of exponents b and a, since they must be the same than the units of $|B_{\text{mix}}| = |B_\phi|^b |A_\phi|^a$ to ensure coherence in Equation (10).
[d] Threshold value B^* unavailable from MD2014.
[e] As determined in Paper I, where the initial interval were $u_0 \in [5, 30]$ m s^{-1}, $\eta_R \in [10^2, 10^4]$ km^2 s^{-1}, and $\tau_R \in [2^1, 2^5]$ years. The linear correlation between u_0 and η_R obtained from the surface analysis should still be considered in conjunction with the final results given in the rightmost column.
[f] As opposed to the optimal intervals obtained in Paper I, where $w = 8 \pm ^{24}_{4}$, $v = 2.0 \pm ^{1.5}_{1.0}$, and $q = (2.8 \pm ^{2.0}_{1.1}) \cdot 2^{1.25(\log_2 v)^2}$.
[g] $\tau_R \gtrsim 32$ years is similar to removing term $-B_R/\tau_R$ in Equation (8).

3.1. Validation with the MD2014 Model

The large number of model parameters listed in Table 1 results from the very general forms adopted for many model

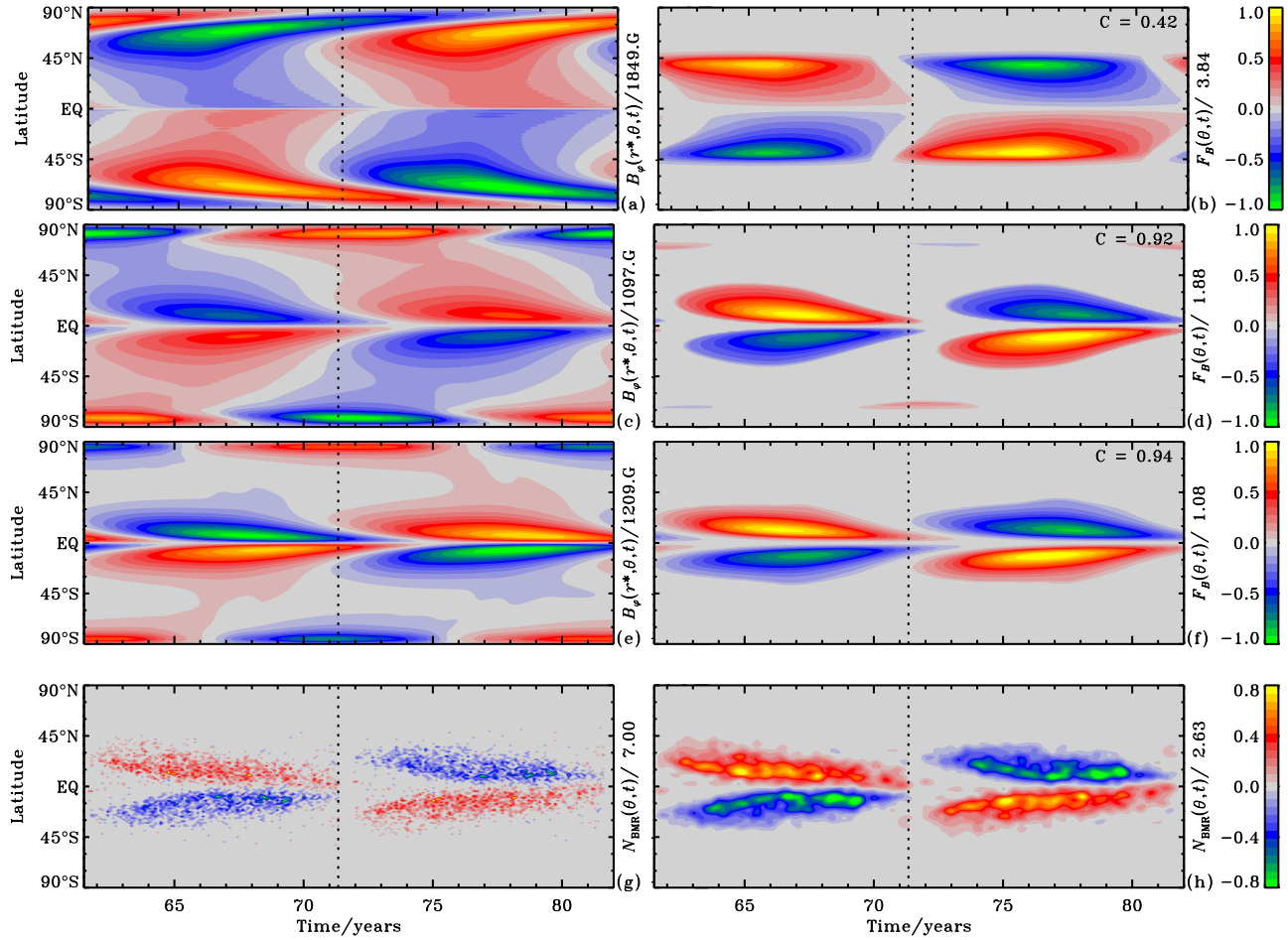

Figure 1. Left: time–latitude contour plots of the toroidal magnetic field component $B_\phi(r^*, \theta, t)$, at $r^*/R = 0.68$, for (a) a two-cycle reference solution approaching that by MD2014, (c) an example of an acceptable solution with $C = 0.92$, and (e) an optimal solution ($C_{\max} = 0.94$). (g) Raw density plot of observed BMRs, extracted from Wang & Sheeley's (1989) database, where all emergences in a given hemisphere and cycle have been attributed the same polarity. Right: (b), (d), and (f) time–latitude contour plots of the emergence function $F_B(\theta, t)$ associated with each of the solutions presented at the left, with their respective fitness factor C. (h) Smoothed version of the density plot presented at the left. All diagrams show the last quarter of simulations W21 × 8 (last two repetitions of cycle 21), which was used for optimization. Time, given in years, starts at the beginning of the eight-cycle runs. Vertical dotted lines indicate the times of activity minima.

ingredients, notably the meridional flow profile and emergence function. This gives the model great flexibility, in that it includes as a subset a number of published models. As an example and a form of validation exercise, we now reproduce a dynamo solution resembling that presented in MD2014.

Since MD2014's model includes a full two-dimensional representation of the solar surface and an emergence algorithm similar to ours, direct contact is allowed between specific features of the two models despite significant differences in algorithmic implementation and numerical procedures. Their (single-cell) meridional circulation profile (described in Dikpati 2011) and magnetic diffusivity profile (described in Dikpati & Gilman 2007) may be closely approached by ours, through the parameter values listed in the first column of Table 1. Similarly, their emergence function is comparable to the one we describe in Section 2.4.2, with a latitudinal masking approximated by parameters $\mu_\ell = 0$ and $\ell^* = 45°$ (a low-latitude cutoff conducive to the production of a solar-like butterfly diagram but hard to justify from the point of view of stability of thin flux tubes) and applied only to the B_ϕ component evaluated near depth $r^*/R = 0.705$. The magnetic masking includes a lower threshold B^* of unspecified value and apparently no upper saturation threshold (parameter $c = 1$). The detailed parameterization of individual emerging BMRs nonetheless differs significantly from ours, in a generally more deterministic manner. The latitude of emergence is directly associated with the location of the peak toroidal field, as compared to the probabilistic approach we use. The tilt, separation, size, and flux of the spot pair are mainly determined by the value of B_ϕ and the latitude of emergence, and so are deterministic rather than stochastic.

In order to minimize the differences associated with stochastic realizations of our emergence procedure, we limit this exercise to the input of observed emergences. Following Paper I, we use the comprehensive database of over 3000 BMRs gathered by Wang & Sheeley (1989) for cycle 21. By feeding these data into Equations 11(a) and 11(b), the 2 × 2D simulation is indirectly forced to run in a cycle-21-like mode. The remaining model parameters are set to mimic MD2014's model (first column of Table 1). We obtain the two-cycle solution presented in Figure 1(a), for the synoptic evolution of B_ϕ at the base of the convection zone. This solution resembles MD2014's result in that it presents a strong mid–high-latitude poleward branch. Our low-latitude equatorial branch is however much weaker. Applying the appropriate latitudinal and magnetic mask from MD2014, we obtain the emergence function, or equivalently the probabilistic distribution of emergences, presented in Figure 1(b). This resembles

the pattern of emergence produced in MD2014, with surface emergences strongly localized around ±40° latitude, with a hint of equatorward propagation (see their Figure 2(a), keeping in mind that the slanted thick poleward streaks going from mid to high latitudes on this time–latitude plot reflect post-emergence SFT, not emergence per se).

3.2. Numerical Optimization

We now seek to select model parameter values so as to obtain a solar-like dynamo solution. This defines a numerical optimization task which consists in optimizing the 18 parameters listed in Table 1 to yield the closest possible fit to solar observations.

The first choice to be made is the goodness-of-fit measure to be used to drive such optimization. We opted to use a single fitness measure, namely the value of the linear correlation coefficient C between the synoptic distribution of synthetic and observed emergences of BMRs. This presupposes that the magnetic flux tubes producing BMRs upon emergence through the photosphere rise radially through the convection zone, on a timescale very much shorter than the cycle period. Models based on the thin flux tube approximation support this idea, at least for the more strongly magnetized flux tube presumably producing the larger BMRs (see, e.g., Fan 2009, and references therein).

Next we must select a suitable observational data set against which to optimize the model. As for the preceding validation exercise, we use Wang & Sheeley's (1989) BMR database for cycle 21. In order to minimize any influence of the initial condition (solar minimum-like dipolar configuration, as introduced in Paper I), we generate a sequence of eight replicates of the cycle 21 database (hereafter W21 × 8), by sequentially inverting the latitudes of emergence from one replication to the next, and use the output corresponding to the last two cycles to compute the correlation coefficient.

3.3. Genetic Algorithm (GA): PIKAIA

We perform the numerical optimization of C using the GA-based optimizer PIKAIA[3] 1.2 (Charbonneau & Knapp 1995; Charbonneau 2002). GAs allow for an efficient and adaptive exploration of the parameter space, and are thus quite robust at handling global optimization problems. As described in Paper I, they also allow for a quasi-Monte Carlo sampling of the parameter space about the current optimum solution, thus helping to construct error estimates on optimal parameter values. In the present context PIKAIA is operating in an 18-dimensional parameter space (see Table 1), with the fitness measure given by the correlation C. Calculating the fitness of a single trial solution (18-parameter vector) implies running the SFT and FTD simulations in parallel, with appropriate coupling through the surface boundary condition, and finally evaluating C. For our working spatial mesh and time stepping this requires about twenty minutes on a single-core modern CPU. For a typical optimization run of 500 generations with 96 trial solutions per generation, this adds up to 667 core-days, but the fitness calculation being almost trivial to parallelize across the population, the wall-clock time can be brought down to a few days.

[3] http://www.hao.ucar.edu/modeling/pikaia/pikaia.php (2015 March).

3.4. Choosing Parameter Ranges

PIKAIA is designed to carry out optimization in a bounded parameter space. The intervals explored for each parameter (second column of Table 1) are chosen to be physically meaningful and computationally stable. In particular, parameters u_0, η_R, and τ_R are restricted to the intervals found in Paper I to better reproduce surface synoptic magnetograms. Parameters q, v, and w, however, are left free to vary in their original intervals despite the preceding calibration, to allow full exploration of the domain. Diffusivity values η_c and η_t and profile parameters δ_c, R_b, and p are given broad intervals but still within limits inferred by theoretical considerations and numerical experiments. Masking parameters are allowed to vary within ranges inferred from calculated stability diagrams, as described in Section 2.4.2.

3.5. Optimal Solution for Cycle 21

The first sequence of optimizations are run with all 18 unconstrained parameters allowed to vary freely in the intervals listed in Table 1, hence called W21 × 8–18. We first analyse the model's behavior relative to the parameters involved in the very definition of the emergence function $F_B(\theta, t)$ (Equation (10)). Figure 2 illustrates the value of the goodness-of-fit C as a function of emergence parameters r^*, b, a, c, B^*, ℓ^*, and μ_ℓ for a set of 192,000 solutions obtained from four independent optimizations (different seed populations), 500 generations each, 96 trial solutions per generation. In all four optimizations, the fitness reaches the same optimal value $C_{\max} = 0.94$. Such optimal solution, which parameters are listed in bold font in the rightmost column of Table 1, is presented in Figures 1(e) and (f). The fit between the emergence function (Figure 1(f)) and the smoothed butterfly diagram of cycle 21 emergences (Figure 1(h)) is good, with expected butterfly shapes and cycle overlaps.

However, it is clear from Figure 2 that considering only a single optimal solution is insufficient, optima being surrounded by a wide variety of sub-optimal but likely acceptable solutions, besides the clearly unacceptable ones. Also, all seven parameters presented are not equally constrained by the fitting procedure. By looking at all solutions standing above the $C \geqslant 0.935$ level (thick black line), we get a first estimate of the relative restriction applied on each parameter. For instance, parameters r^*, a, and B^* are fairly well constrained to a limited interval within the original boundaries, while parameters b, c, ℓ^*, and μ_ℓ show wider regions of acceptable fit.

In order to build meaningful error estimates for each parameter, we must assess the physical limit of validity of the optimization criterion. Clearly, there must exist a value of C above which solutions are physically acceptable, even if not strictly optimal. An example of such a solution, with $C = 0.92$, is presented in Figures 1(c) and (d). The butterfly shape in this solution is still clearly visible, though a second tail is starting to build toward the high latitudes. These differences are significant enough to declare such a solution inferior to the optimal one, but still at the limit of acceptability in terms of observed global features. The horizontal blue lines in Figure 2 delimit the solutions that are characterized by a criterion $C \geqslant 0.92$.

Before proceeding further into the parameter analysis, we now opt to get rid of the variability associated with the definition of the empirical emergence function (Equation (10)),

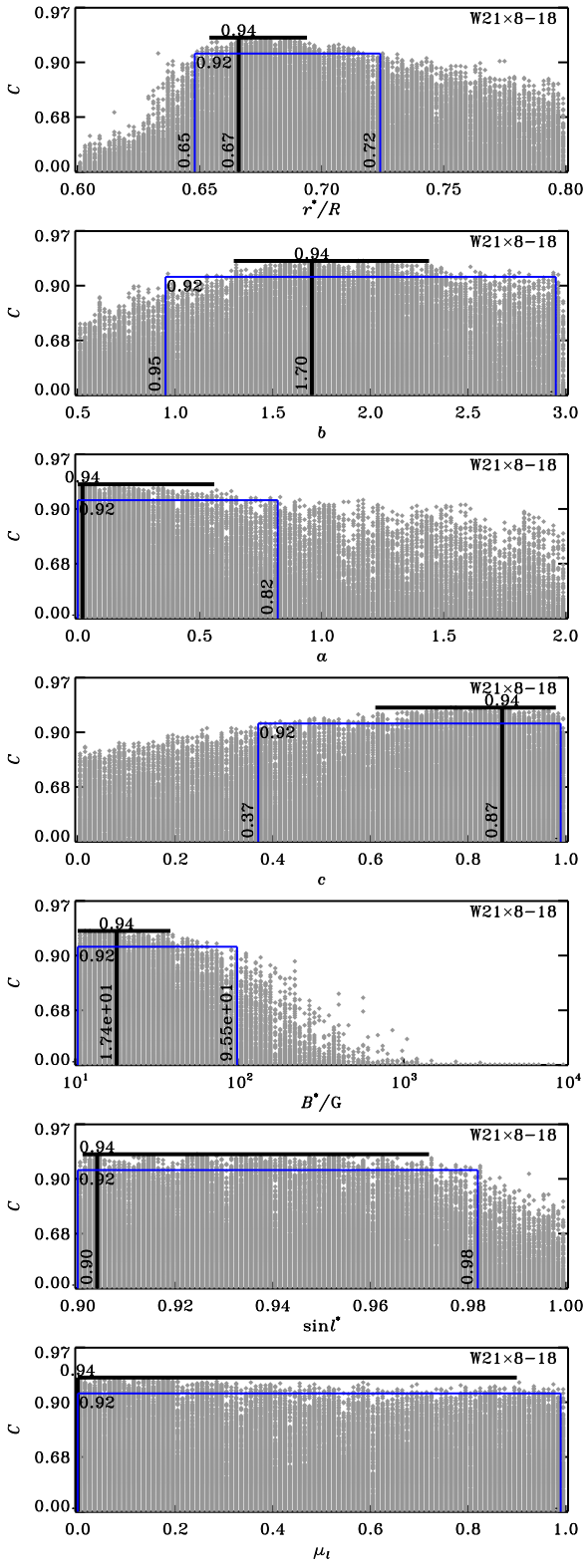

Figure 2. Distribution of the fitness C (vertical inverse log scale) as a function of each of the seven "emergence" parameters (r^*, b, a, c, B^*, ℓ^*, and μ_ℓ). Each gray dot indicates the parameter-space position of one of the 192,000 solutions obtained from four independent W21 × 8–18 optimizations. The remaining eleven parameters are not shown here since their final analysis is based instead on the W21 × 8–11 optimization (see Figure 4). On each plot, the thick horizontal line indicates the interval where $C \geqslant 0.935$, and the thick vertical line the parameter value where true maximum fitness $C = 0.94$ is reached. Thin vertical blue lines delimit the parameter values where fitness reaches $C = 0.92$, such that any solution above the horizontal blue line is considered acceptable.

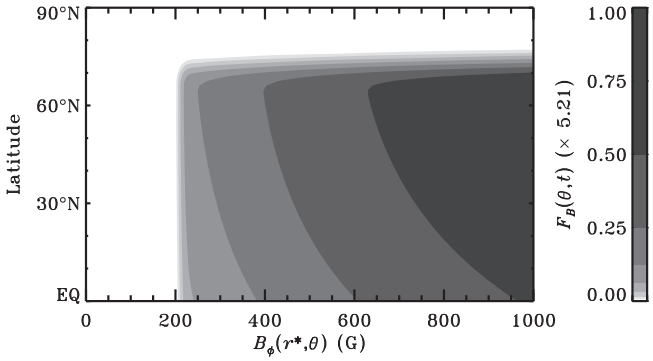

Figure 3. "Stability diagram" used as a mask on the toroidal magnetic field component $B_\phi(r^*, \theta, t)$ shown in Figure 1(e), to produce the emergence function $F_B(\theta, t)$ shown in Figure 1(f). This corresponds to Equation (10) with $\delta B^* = 10^{-1} B^*$, and parameters b, a, c, B^*, ℓ^*, and μ_ℓ set to their final values, as listed in the rightmost column of Table 1.

and pick up definitive values, within the interval of acceptability, for the parameters involved. The inferred depth for the generation of flux instabilities is thus set near its optimal value $r^*/R = 0.68$, by averaging the magnetic field values between $r/R = 0.68$ and 0.70. For simplicity, the relative contribution to $B_{\rm mix}$ of the poloidal field is set to zero ($a = 0$), while we round the optimal exponent of the toroidal contribution to $b = 1.5$. The lower threshold, above which this diffuse toroidal field is assumed to be able to generate instabilities, is set to its highest acceptable value, that is $B^* = 10^2$. The units of B^* are in fact $\mathrm{G}^{1.5}$ in the case $b = 1.5$ to ensure coherence in Equation (10). This corresponds to a lower threshold of $\simeq$200 G in B_ϕ, as illustrated in Figure 3. The emergence function F_B remains proportional to $B_{\rm mix}$, with $c = 1.0$, rather than saturating above B^*. The highest latitude of emergence is fixed to $\ell^* = 70°$ ($\sin \ell^* = 0.94$), in accordance with stability diagrams by Ferriz-Mas et al. (1994), and the equatorial intercept μ_ℓ is set to 0.5, such that the latitudinal filter halves smoothly from $\ell^* = 70°$ down to the equator. The final emergence function (i.e., emergence probability) can now be mapped as a function of latitude and toroidal field amplitude, as shown in Figure 3, to form a synthetic "stability" diagram, which is the model's equivalent to the stability diagrams presented in Ferriz-Mas et al. (1994, Figures 1 and 2).

With the emergence function now fixed, we carry out a new series of four optimizations, hereafter called W21 × 8–11, with only the 11 physical model parameters (δ_c, R_b, u_0, p, q, ν, w, η_c, η_t, η_R, and τ_R) left to vary freely in their prescribed intervals. The corresponding 192,000 solutions are presented in Figure 4 as a function of each parameter value. Again, the optimal fitness reaches $C_{\rm max} = 0.94$, and all solutions characterized by a $C \geqslant 0.92$ are considered acceptable. The corresponding interval for each parameter is used to define final error bars about the optimal values, as listed in the rightmost column of Table 1. As mentioned earlier, various combinations of parameters within these accepted intervals lead to acceptable solutions, but not all do, due to various correlations between some pairs of best-fit parameters (see also the discussion in Paper I, Section 3.5). Figure 5 depicts two of the strongest such correlations uncovered in our W21 × 8–11 set of solutions. The left panel shows a net linear (anti)correlation between the surface meridional flow speed u_0 and one of the parameters (p) setting the depth dependence of the meridional flow in the interior (see Equation 3(a)). This (anti)correlation has an unambiguous physical explanation: it leads to all solutions near

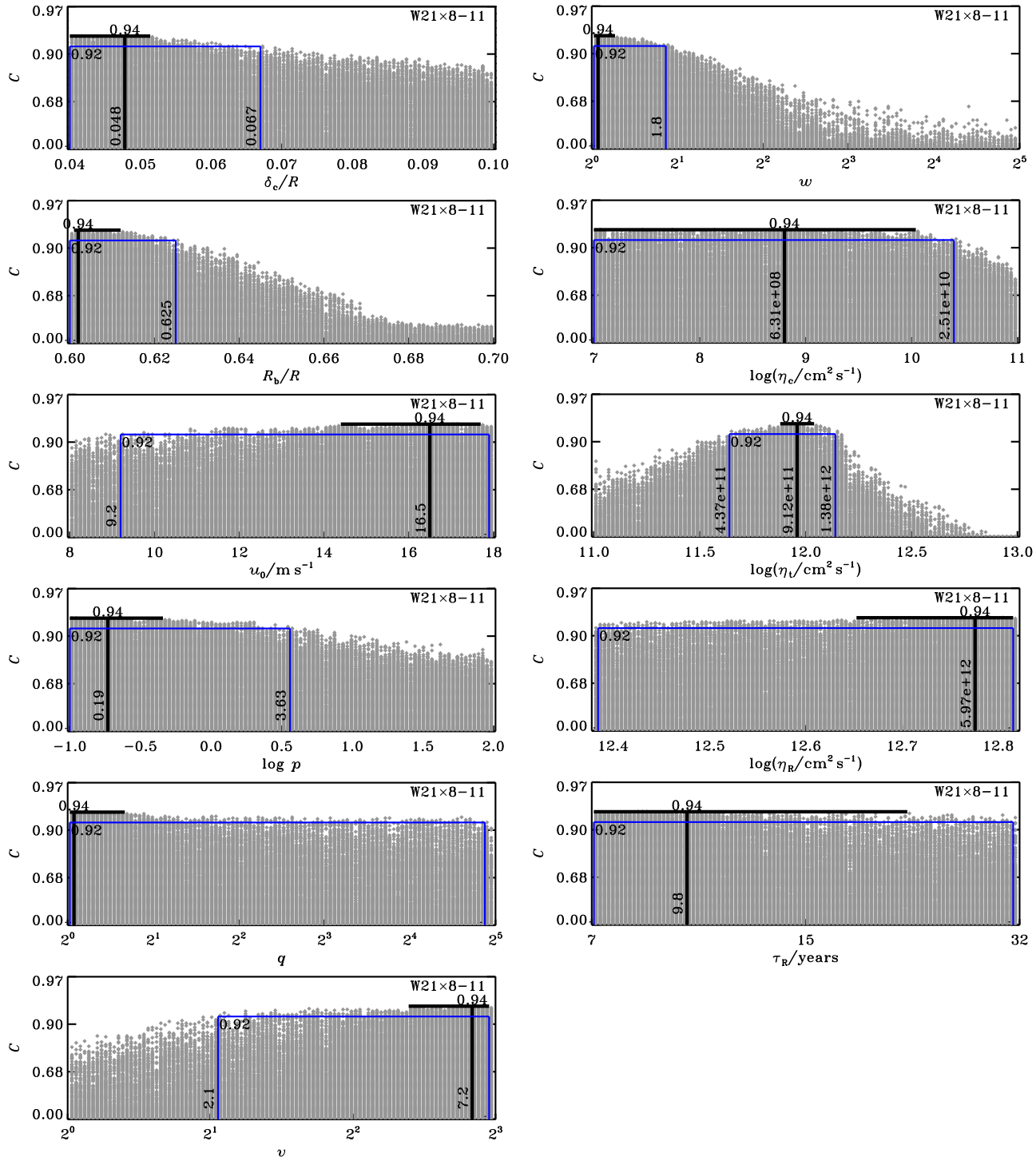

Figure 4. Same as Figure 2, but for the eleven model parameters (δ_c, R_b, u_0, p, q, v, w, η_c, η_t, η_R, and τ_R), from four independent W21 × 8–11 optimizations, while the seven "emergence" parameters are held fixed to their optimal value listed in Table 1.

the red line having an equatorward meridional flow speed equal to 6.6 m s^{-1} ± 8% at $r/R = 0.66$, that is below the base of the convective envelope, beneath the layer where the emergence function is calculated. It is the speed of this return flow that sets the cycle period, and thus is strongly constrained by the sunspot butterfly diagram used to establish our goodness-of-fit measure. The right panel of Figure 5 shows another correlation between a pair of parameters, in the form of a somehow triangular constraint on parameter q, which controls the polar end of the latitudinal dependence of the meridional flow, as a function of maximum flow speed u_0 (see Equation 3(b)). This correlation sets a lower limit on the surface flow speed at mid–high latitude, of the order of $\gtrsim$5 m s^{-1}.

4. A SOLAR-LIKE DYNAMO SOLUTION

Now that the physical model and masking parameters have been properly calibrated to ensure that function $F_B(\theta, t)$ reproduces the observed solar butterfly diagram of surface emergences, we may use it as the statistical emergence function

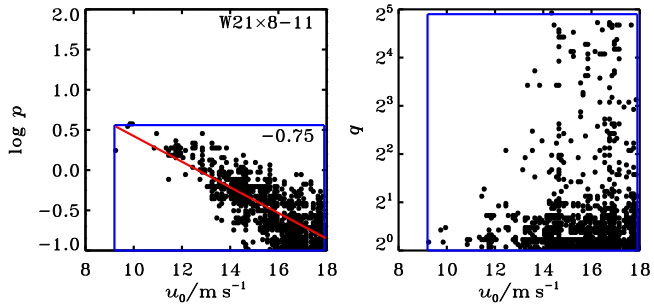

Figure 5. Correlations between the best-fit parameter values for surface meridional flow speed u_0 and (left) depth variation parameter p and (right) latitudinal profile parameter q (see Equations 3(a) and 3(b)). The blue squares correspond to the $C \geqslant 0.92$ regions on Figure 4, third, fourth, and fifth panels on the left. The linear best-fit (red line) and Pearson's correlation coefficient are also shown on the left panel. In particular, despite the ranges of values for u_0, p, and q, all these solutions have a peak equatorward flow speed of 6.6 m s^{-1} ± 8% near $r/R = 0.66$.

it was meant to be, i.e., providing the missing surface source term $S_{\rm BMR}(\theta, \phi, t)$ with new emergences generated from deep seated toroidal flux (Equations 11(a) and 11(b)) and thus closing the loop for a self-consistent and autonomous 2 × 2D dynamo.

In all following cases, we use as initial condition the simulation state at the end of the previously calibrated W21 × 8 sequences. This ensures that the new simulations start up from a state representative of a solar activity minimum.

4.1. Quasi-linear Regime

The linearity in $\boldsymbol{B}$ of the FTD Equations 7(a) and 7(b) and SFT Equation (8) is expected to lead to either growing or decaying dynamo solutions. In the well-studied mean-field framework, this behavior is controlled by the "dynamo number." Here it is the proportionality constant K between $F_B(\theta, t)$ and the absolute number of emerging BMRs per time step that play the equivalent role. Since $a = 0$ and $b = 1.5$ in the definition of $B_{\rm mix}$, and $c = 1$ in Equation (10), the number of emerging BMRs is proportional to $B_\phi{}^{1.5}$ as long as the latter exceeds the lower threshold B^*. However, the emergence process itself is inherently stochastic, so the dynamo growth rate can only be defined in a statistical sense, hence the "quasi-linear" labeling.

The top panel of Figure 6 depicts the temporal evolution of the total magnetic energy content inside the simulated Sun, for ≃8-cycles sample realizations of a 2 × 2D dynamo run in the quasi-linear regime at four different dynamo numbers K. From these few samples, the transition between decaying (small K) and exponentially growing (large K) solutions seems sharp, but a more complete analysis reveals otherwise. The middle panel of Figure 6 shows how the growth rate of the magnetic energy can show a wide spread at a given value of K. Error bars on the plot illustrate the intervals of growth rates obtained at each given K, through ten different realizations of the statistical emergence procedure described earlier (see Section 2.4.2). We also performed a similar set of simulations in a reduced stochastic regime (shown in black on the plot). This reveals the strong global impact of stochasticity in the emergence process, particularly by the distributions in separations and tilts of emerging BMRs. The consequence is that a precise value for the critical dynamo number cannot be defined, with different realizations of the dynamo with $K \in [0.4, 0.6]$ resulting in

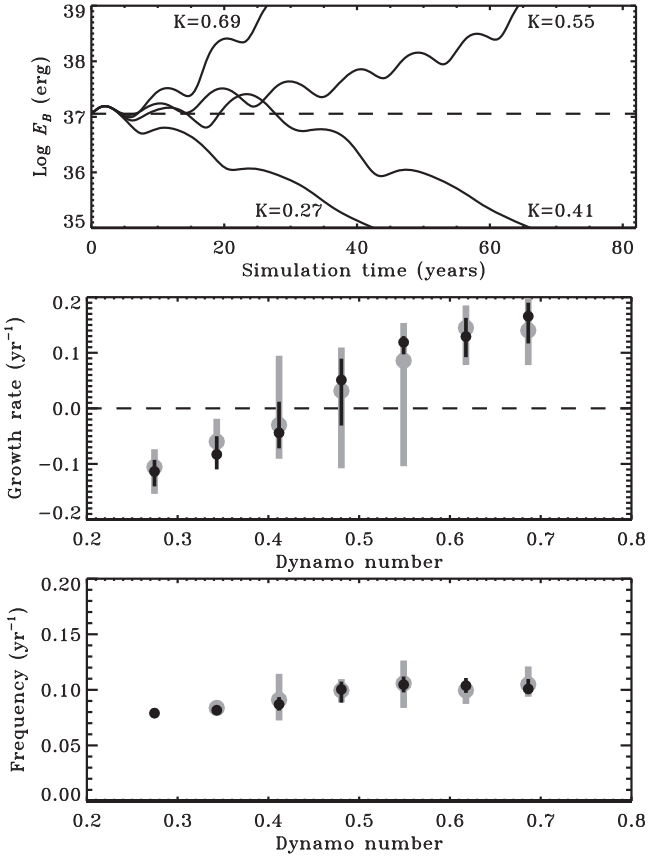

Figure 6. Top panel: evolution of the total magnetic energy content inside the simulated Sun, for ≃8-cycles sample realizations of a 2 × 2D dynamo run in the quasi-linear regime at four different dynamo numbers K (horizontal dashed line indicates the initial energy level). Middle panel: long term growth rate of the magnetic energy as a function of dynamo number K, for ten independent realizations of (thick gray) the full statistical emergence procedure (see Section 2.4.2, stochasticity sources (i) to (vi)) per value of K and of (thin black) a reduced stochastic emergence procedure (retaining sources (i) to (iv) only, and fixing bipole separations (v) and tilts (vi) at their observed mean values). Bottom panel: similar as the preceding panel, but for the oscillation frequency of the detrended magnetic energy.

dynamo solutions that can either grow or decay. The fact that this transition region lies significantly below the value $K \simeq 1$ required to reproduce the observed butterfly diagram for cycle 21 in the preceding section suggests that the dynamo should run in the supercritical regime, with some nonlinear feedback regulating the mean cycle amplitude. This aspect will be discussed in the following subsection.

As another indicator of the model behavior, average cycle frequencies (periods) of the corresponding solutions, are also presented in the bottom panel of Figure 6, again with error bars showing the intervals of frequencies obtained for a given K. Considering the difficulty of measuring cycle periods in quickly decaying oscillatory solutions (low K), no strong trend appears from this plot. This suggests how robust the model is at producing oscillations on a 9–12 years timescale, in spite of the strong variability associated with stochastic processes.

4.2. Tilt-quenching and Reference Dynamo Solutions

To overcome the problem of (quasi-)linearity, but without dealing explicitly with dynamical feedback, some ad hoc quenching may be added to the dynamo source terms.

Motivated by the modeling of the buoyant rise of thin magnetic flux tubes by D'Silva & Choudhuri (1993) and Caligari et al. (1995) (for a review see Fan 2009, Section 5.1.2, and references therein), we introduce a quenching of the BMR mean tilt as a function of the amplitude of the contributing underlying toroidal field $B_\phi(r^*, \theta, t)$, in order to mimic the resistance of magnetic tension in strongly magnetized flux tubes against the twisting imparted by the Coriolis force. Observationally the situation is less clear-cut (see Section 6 in Pevtsov et al. 2014 for a recent review). Dasi-Espuig et al. (2010) and McClintock & Norton (2013) do find an influence of cycle amplitude on mean tilt angles, varying from cycle to cycle and from one solar hemisphere to another, but Stenflo & Kosovichev (2012) do not find a statistically significant relationship between tilt angles and flux of individual BMRs.

The quenched tilt is written as

$$\alpha_q = \frac{\alpha}{1 + (B_\phi/B_q)^2}, \tag{12}$$

with B_q some ajustable critical magnetic field amplitude. In the context of the present dynamo model, we find a tilt-quenching with $B_q \simeq 500$ G, at dynamo number $K = 0.75$, to be adequate to generate stable dynamo solutions, comparable to solar amplitudes for the butterfly density plot and the monthly number of newly emerged BMRs. The latter we refer to as a "pseudo-SSN," since no consideration is given here to distinguishing groups versus individual emergences, or assigning them different weights, as is the case in the definition of the international SSN. For instance, observed cycle 21 peaks at a SSN of $\simeq$175 while the maximum monthly number of newly emerged BMRs in Wang & Sheeley's (1989) database is $\simeq$50.

Figures 7(b)–(g) illustrate the evolution of the deep toroidal field, total magnetic energy, BMR density, pseudo-SSN, surface radial field, and axial dipole moment for a sample dynamo solution run over more than 300 years and roughly 32 synthetic solar cycles. The temporal series exhibit solar-like behaviors in many aspects, in particular cycle periods varying between 8.5 and 12 years, cycle amplitude variations of a factor three to four in the pseudo-SSN, and long term variability such as some progressive increase of cycle amplitude after the occurence of a weak cycle or the triggering of small cycles after very strong ones. Some significant hemispheric asymmetries are also noticeable on the various plots, but polarity reversals remain sharply synchronized, indicating strong cross-hemispheric coupling. The oscillating surface axial dipole moment peaks at or near the pseudo-SSN minimum, in agreement with observations. The phase relationship between the surface dipole and deep-seated toroidal field is also solar-like, with the dipole peaking at or shortly prior to the pseudo-SSN minimum.

The overall amplitude of this dynamo solution is, however, slightly higher than that of the average solar cycle. The axial dipole moment (panel (g)) oscillates with an amplitude of $\simeq 10$ G $\cdot R^2$ as compared to $\simeq 4$ G $\cdot R^2$ for the Sun. The pseudo-SSN (panel (e)) peaks between $\simeq$50 and $\simeq$150, which is slightly higher than average solar cycle amplitude ($\simeq$50 for cycle 21). This corresponds to 50–150 emergences per month near cycle maxima down to 0–10 per month at cycle minima. The total number of BMRs to emerge during a cycle varies from $\simeq$2000 for the smallest cycles to $\simeq$8000 for the strongest ones, which is comparable, but again slightly higher on average, than the original $\simeq$3000 BMRs extracted from Wang & Sheeley's (1989) database for cycle 21. Due to the use of a constant log-normal distribution for BMR magnetic fluxes, total magnetic flux emerging during a cycle scales linearly with the number of BMRs. Finally, most presumably due to the use of a suboptimal profile for the surface meridional circulation leading to extra flux accumulation near the poles at activity minima, the peak amplitude of the radial surface field (panel (f)) builds up at an order of magnitude stronger than observed. At any rate, a dynamo number $K \lesssim 1$ is more than sufficient to maintain stable dynamo solutions, with only the BL mechanism operating and without having to artificially enhance the emerging flux (see also Cameron & Schüssler 2015). The value of K used here for the reference dynamo should even be brought down a little to better fit solar cycle observations.

Also shown in Figure 7(a) is a series of radius–latitude cuts of the toroidal field component, at nine different phases of a synthetic sunspot cycle. The toroidal field reverses amplitude after $\simeq$9 years, which is slightly shorter than the average observed sunspot cycle. The peak toroidal field amplitude near $r/R = 0.7$ is reached at mid-cycle, near maximum sunspot activity. Below the tachocline, the magnetic field from three to four successive cycles piles up to thinner and thinner layers as it reaches the depth $r/R = 0.6$. This is precisely what is to be expected from the average diffusivity $\eta \simeq 5 \times 10^{10}\,\mathrm{cm^2\,s^{-1}}$ used at $0.6 \geqslant r/R \geqslant 0.7$, which corresponds to a diffusive timescale of $\simeq$31 years. Below $r/R = 0.6$, the magnetic diffusivity of $10^9\,\mathrm{cm^2\,s^{-1}}$, leads to a diffusive timescale $\gtrsim$1000 years. Therefore, while the meridional circulation acts on a timescale commensurate with the sunspot cycle period, the deep diffusive processes act on much longer timescales. The remnants from old cycles appear to be able to feed back into the dynamo system and induce some long-term memory in cycle amplitude.

Figure 8 shows some long-term interrelations between cycle properties, extracted from the preceding dynamo solution. Panel (c) in the figure shows the strong linear correlation (0.89) obtained between amplitude (maximum pseudo-SSN) of a cycle (n) and maximum axial dipole moment at the end of the preceding cycle ($n - 1$). This behavior is to be expected from the quasi-linear transport and shearing of the poloidal magnetic field accumulated at cycle minimum into a deep toroidal component peaking at cycle maximum and generating a proportional number of surface emergences. As shown in panel (d) of the figure, the reverse correlation is not true, however, as the stochastic properties of emerged BMRs during a given cycle n destroy the otherwise expected correlation between pseudo-SSN and axial dipole amplitude at the end of the same cycle (n). Also, even if long-term magnetic memory does exist in the interior, the poor correlations obtained between amplitude of cycle n and axial dipole moment at the end of cycles $n - 2$ (panel (b)) and cycles $n - 3$ (panel (a)) indicate that it is erased by the stochasticity of flux emergence. Despite these stochastic sources of fluctuations, hemispheric cycle amplitudes remain strongly correlated, as shown in Figure 8(f). All the preceding results are in good agreement with observed solar cycle characteristics (see, e.g., Muñoz-Jaramillo et al. 2013, Figure 5).

As also shown in panel (e) of Figure 8, cycle amplitude and period are essentially uncorrelated. This differs from the behavior observed in the Sun, where a significant anticorrelation is inferred between these two cycle measures. Some

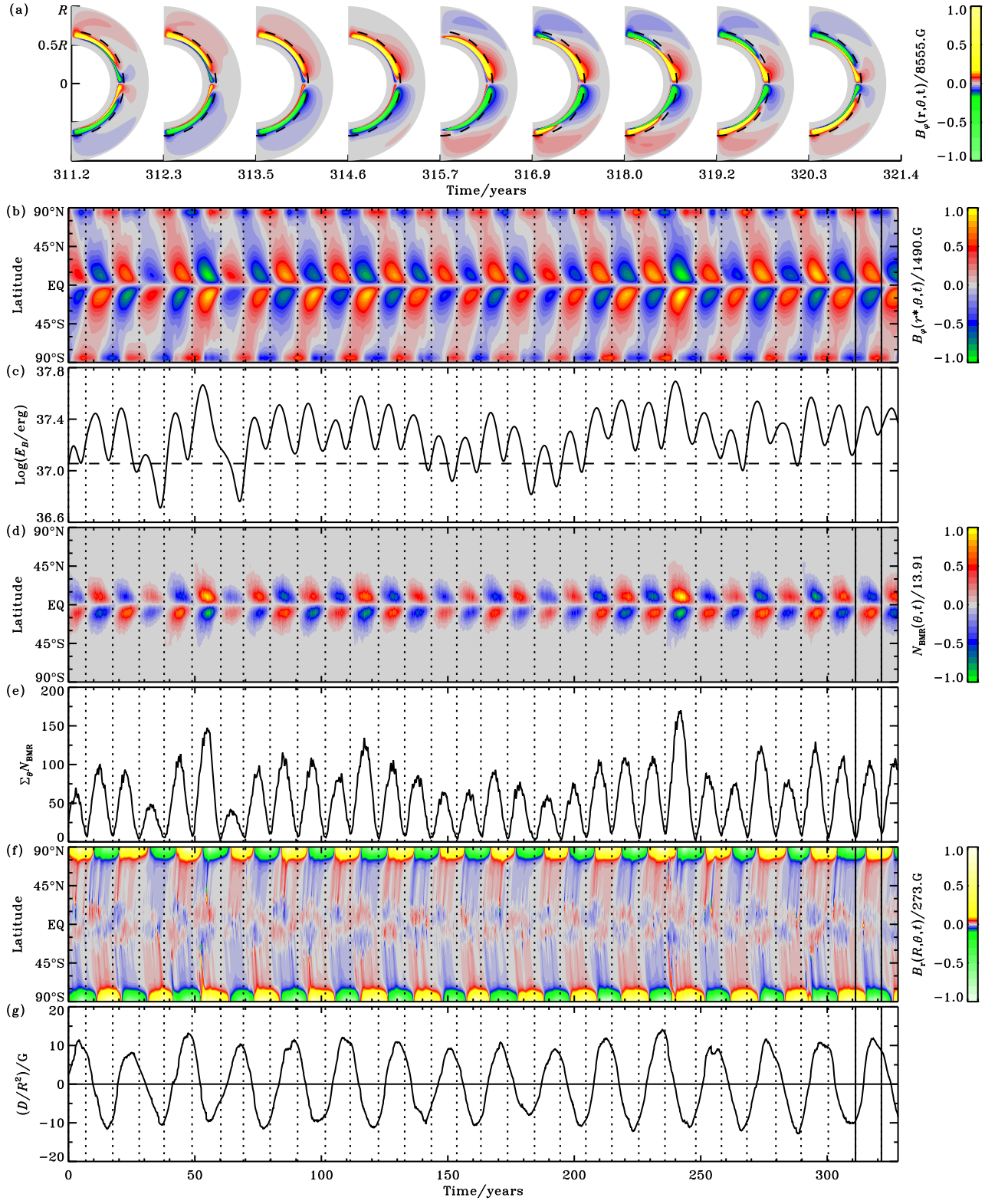

Figure 7. A representative solar-like tilt-quenched 2 × 2D dynamo solution obtained using the optimal parameter values listed in the rightmost column of Table 1. (a) Latitude–radius snapshots of the toroidal magnetic field between $r/R = 0.5$ and 1.0, at nine different phases of the dynamo cycle delimited by two vertical continuous lines in the following plots (color table saturates above 1.5 kG; dashed lines indicate the depth of the tachocline ($r/R = 0.7$)). (b) Time–latitude contour plot of the toroidal magnetic field averaged in the depth range $0.68 \leqslant r^*/R \leqslant 0.70$; (c) corresponding temporal evolution of the total magnetic energy content inside the simulated Sun ($0.5 \geqslant r/R \geqslant 1.0$; horizontal dashed line indicates the initial energy level). (d) Time–latitude density plot (butterfly diagram) of the number of BMRs emerged at the surface, as dictated by the emergence function F_B, in turn based on the preceding toroidal field amplitude; (e) corresponding monthly number of newly emerged BMRs (pseudo-SSN), as a function of time. (f) Time–latitude contour plot of the surface radial magnetic field (color scale saturated above 27 G); (g) corresponding temporal evolution of the surface axial dipole moment. Vertical dotted lines indicate the times of activity minima as defined by the minimum values of the pseudo-SSN.

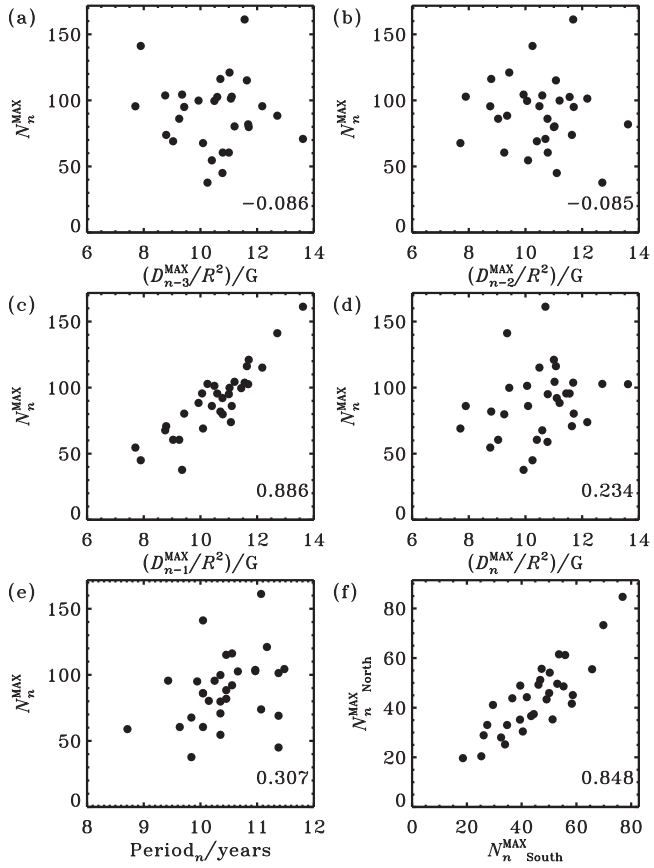

Figure 8. Amplitude (maximum pseudo-SSN) of cycle n as a function of maximum axial dipole moment at the end of (a) cycle $n-3$, (b) cycle $n-2$, (c) cycle $n-1$, and (d) cycle n, for the sample dynamo solution presented in Figure 7. (e) Cycle amplitude as compared to the period of the same cycle. (f) Cycle amplitude calculated independently in each hemisphere and plotted against one another. In each panel is also given the corresponding Pearson's linear coefficient.

additional dynamical feedback would likely be required to reproduce such behavior.

4.3. Long-term Variability

Figure 9 shows the Fourier transforms of the pseudo-SSN time series, for a sample 32-cycle, tilt-quenched 2×2D dynamo simulation similar to the reference solution of Figure 7, along with the average spectra constructed from three statistically independent realizations of a 96-cycle simulation. The relatively poor sampling of the 32-cycle simulation shows spectral features similar to those of the 23-cycle solar SSN spectrum (also shown in the figure), in that it presents a broad peak between periods of 9–12 years (8–14 years for the SSN) as well as low-amplitude (5%–10% of peak power) structures at other frequencies. However, these secondary features occur at different frequencies for the SSN and for different realizations of the pseudo-SSN, and so do not represent physically robust signals. Indeed, the averaging of three 96-cycle spectra (equivalent to $\simeq$300 cycles in total) reveals no hint of a low-frequency signature above 2% of peak power, of the type one would associate with the so-called Gleissberg or Suess cycles detected in temporally extended records of solar activity. The cycle period is also much more robust, at 9.5–11 years. These results indicate that despite the strong

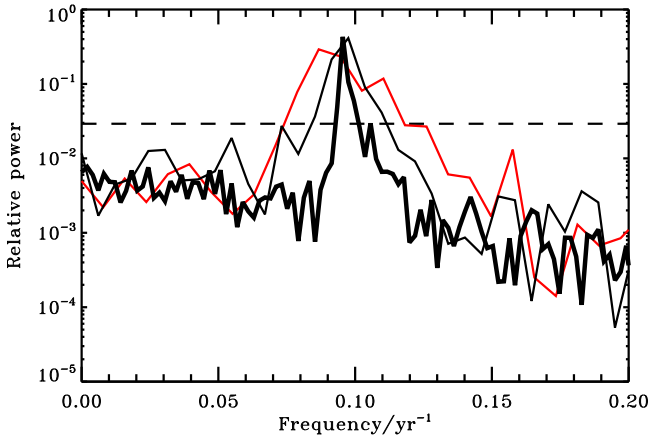

Figure 9. Temporal power spectra of the solar SSN (thin red), of the pseudo-SSN of a sample 32-cycle tilt-quenched 2×2D dynamo simulation (thin black), and of the pseudo-SSN averaged over three independent realizations of a 96-cycle simulation (thick black). In all three cases, the Fourier transform was performed on a signed version of the temporal series, with amplitudes alternatively reversed from one cycle to the next to impose an oscillation about zero, and the frequencies subsequently multiplied by two to retrieve the $\simeq$10 year sunspot cycle characteristic period. The horizontal dashed line marks 10% of the peak spectral power.

variability in cycle amplitude characterizing the simulations, the period is very stable, even more so than in the real Sun.

Figure 10 shows two sets of synthetic butterfly diagrams and associated pseudo-SSN time series, obtained for the same parameter values as the solution of Figure 7 but using distinct stochastic realizations for the fluctuating properties of the synthetic BMRs. The top solution generally resembles panels (d) and (e) of Figure 7 in its overall amplitude fluctuation pattern, but now also shows an episode of strongly reduced cycle amplitude, persisting here for four cycles ($84 \leqslant t \leqslant 132$ years) and reminiscent of the 1796–1825 Dalton minimum of the sunspot record. Entry into this low-amplitude episode is sudden, the preceding few cycles being of average amplitude or higher. Recovery is however more gradual, with a few cycles required for the cycle to build back up to its pre-event average amplitude.

The solution plotted on the two bottom panels of Figure 10 shows yet another interesting behavior: a complete halt of the cyclic dynamo, here at $t \simeq 150$ years, following a sequence of unfavorably positioned and/or tilted large BMRs, leading to a much reduced dipole moment building up in the descending phase of the cycle peaking at $t \simeq 118$ years. Because of the lower cutoff B^* built into our emergence function (see Equation (10) herein), once the toroidal magnetic field falls below this threshold, BMRs are no longer produced, so that the existing dipole then undergoes simple resistive decay, followed by resistive decay of the toroidal component, as per Cowling's theorem. A distinct inductive mechanism able to operate at low mean-field strengths, such as the alpha-effect of classic mean-field electrodynamics, would be needed here to restart the dynamo cycle (see, e.g., Passos et al. 2014). Ongoing numerical experiments along these lines suggest that this would be a feasible path toward the generation of solar-like grand minima of activity.

In a set of 30 realizations similar to the one displayed in Figure 7 and the two in Figure 10, 7 shut off before reaching the 32nd cycle, and 15 before reaching the 96th cycle. The probability of a dynamo to remain active after a certain number of cycles thus decreases with time in a manner that appears

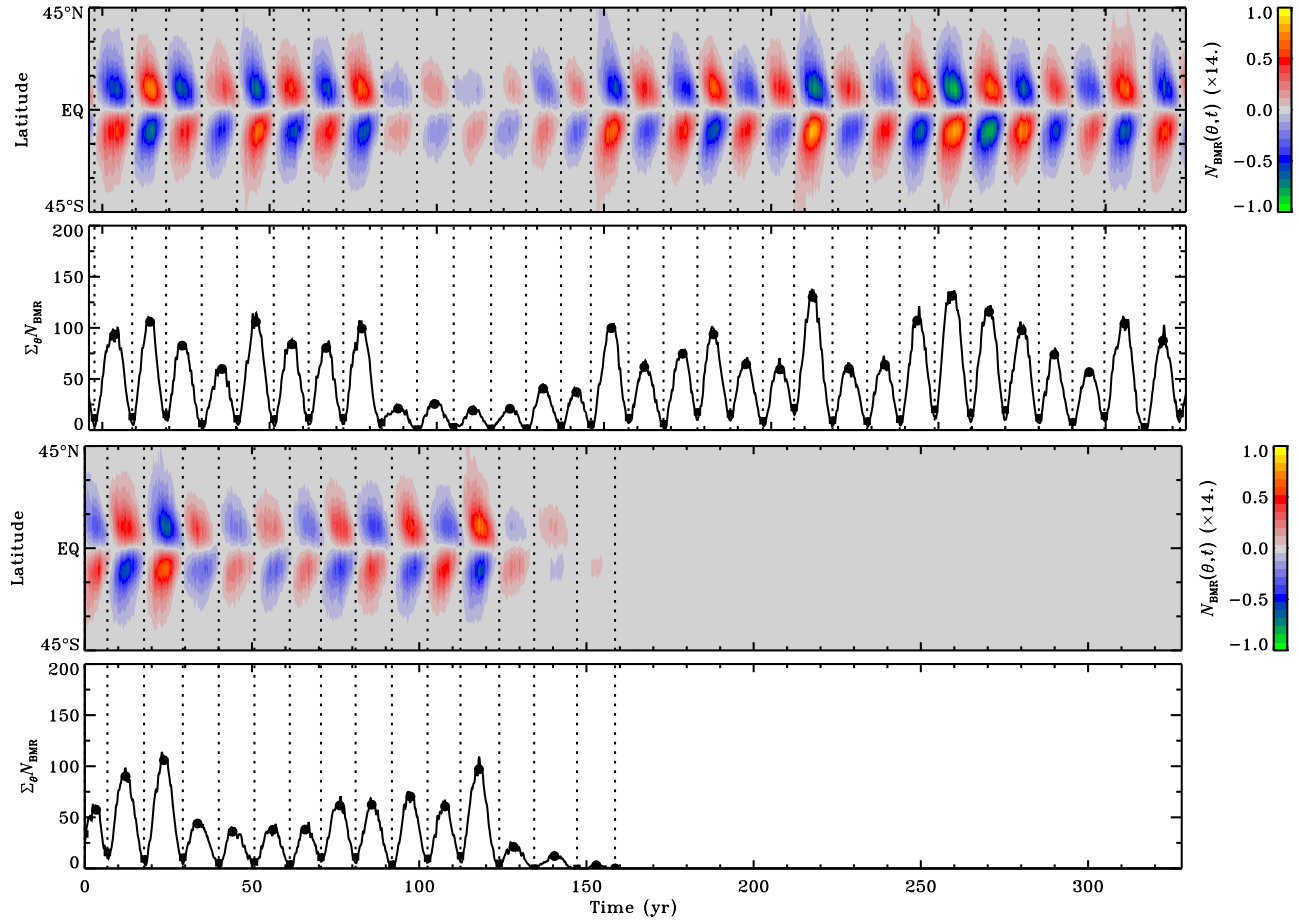

Figure 10. Time–latitude density plot (butterfly diagram) and corresponding monthly number (pseudo-SSN) of newly emerged BMRs, for two distinct realizations of a 32-cycle, tilt-quenched 2 × 2D dynamo simulation using the same optimal parameter values used to produce the reference solution of Figure 7 (see panels (d) and (e)).

consistent with a stationary memoryless random process, as would be expected from the stochastic nature of the properties of emerging BMRs built into the model. A detailed, quantitative investigation of these matters, currently underway, will be the focus of a subsequent paper in this series.

5. DISCUSSION

The dynamo solutions presented above result from the use of a model calibrated to cycle 21 emergence data through an optimization process operating on a specific goodness-of-fit measure and in a bounded search space. These bounds were set (loosely) on observational and/or physical grounds, but obviously pose a restriction on the range of solutions accessible to the optimization. Could we do better than the optimal solution listed in Table 1? We have carried out a number of alternative optimization runs in order to answer this question, as now described.

An 18-parameter optimization similar to that described in Section 3.5, but using much broader ranges of parameter, does manage to return a best-fit solution with $C = 0.97$, significantly better than the original 18-parameter best-fit solution, which has $C = 0.94$. This nominally superior fit, however, is achieved through a low-latitude cutoff for the emergence function, down to $\ell^* = 30°$, which is clearly incompatible with stability diagrams for thin toroidal flux ropes.

We also carried out optimization runs in which the parameters defining the latitudinal dependence of the meridional flow (see Equations 3(a)–3(b)) are constrained to a narrower range of acceptable values, corresponding to the best-fit SFT solution obtained in Paper I by fitting actual synoptic magnetograms, rather than just the spatiotemporal distributions of BMR emergences. The best-fit solution from such an optimization reaches only $C \simeq 0.86$, which is much less satisfactory than the $C = 0.94$ best-fit solution. More worrisome is the fact that the surface meridional flow for the best-fit solution and error bars of Table 1, plotted in Figure 11 (dark gray band), provides a rather poor fit to the Doppler observations of Ulrich (2010), which lie mostly outside the range of acceptable solutions from the optimization run. The best-fit profile of Paper I did much better in this respect (reproduced herein as the pale gray band in Figure 11).

This suggests some incompatibility between the optimization of the SFT model relative to surface magnetograms and the optimization of the coupled SFT–FTD model relative to the shape of the sunspot butterfly diagram. The W21 × 8–11 optimal solution of Section 3.5 still lies within the surface-optimized ranges for the maximum meridional flow amplitude u_0, the surface diffusivity η_R, and the exponential decay time τ_R obtained in Paper I, while the parameters q, v, and w (see Equation 3(b), setting the latitudinal dependence of the stream function, do not. Interestingly, despite significant variations in latitudinal profiles, all acceptable solutions ($C \geqslant 0.92$) have a peak equatorward meridional flow speed of 6–7 m s^{-1} near the base of the circulation cell; this is consistent with the deep

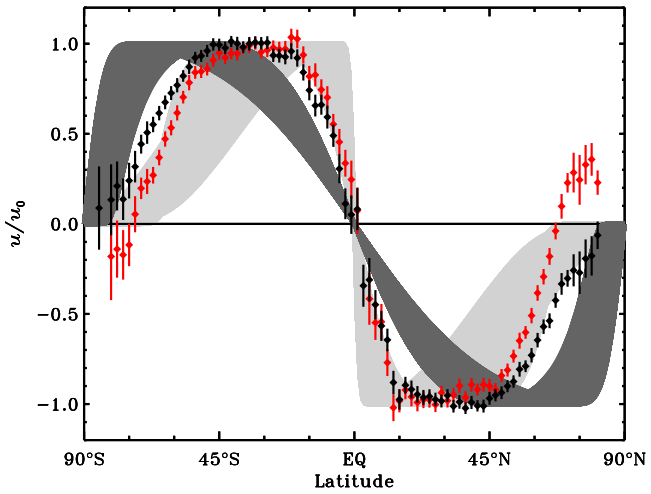

Figure 11. Observed and modeled latitudinal profiles of surface meridional flow. The dark gray band indicates the range of acceptable profiles in the W21 × 8–11 optimal solution of Section 3.5, while the pale gray band indicates the acceptable range obtained in Paper I by fitting the full synoptic magnetograms. The solid dots and error bars are the Doppler measurements of Ulrich (2010) for cycles 22 (red) and 23 (black).

meridional flow setting the cycle period in these dynamo solutions, which leads to a very tight constraint when fitting the butterfly diagram.

The analytic form adopted here for the meridional flow stream function is of course extremely simple: steady and separable in r and θ, which enforces the same latitudinal dependence at all depths, and defining a single flow cell per meridional quadrant. What our butterfly diagram-based goodness-of-fit measure thus constrains is primarily the flow at the base of the convection zone. The misfit with the results from purely surface optimization suggests that the internal flow is more complex than the single-cell profile used here. Indeed, the recent helioseismic inversions of Zhao et al. (2013) and Schad et al. (2013) suggest multiple cells in radius, which is known to have a large impact on the operation of FTDs (e.g., Jouve & Brun 2007). The dynamo modeling work of Hazra et al. (2014a) indicates, however, that provided additional transport processes such as turbulent diffusion and/or pumping can couple the surface and base of the convection zone, solar-like butterfly diagrams can be produced as long as an equatorward flow is present at or immediately beneath the base of the convection zone (see also Jiang et al. 2013).

Another physical inconsistency of the W21 × 8–11 optimal solution is the meridional flow's deep penetration below the base of the convection zone. This is known to be conducive to the production of solar-like butterfly diagrams (e.g., Nandy & Choudhuri 2002), but unlikely on dynamical grounds (Gilman & Miesch 2004), and delicate to reconcile with observed solar light element abundances (Charbonneau 2007). Finally, both observations (Ulrich 2010) and numerical simulations (Passos et al. 2012) suggest that the meridional flow may undergo systematic temporal variations in the course of the cycle, presumably driven by the cycling magnetic field. Such effects are a priori excluded from the meridional flow parameterization used here.

All these incompatibilities and inconsistencies most likely reflect, at least in part, the specific choices made for the parameterization of the meridional flow profile. An interesting possibility would be to use our GA-based fitting technique to invert a spatially resolved discretization of the internal meridional flow from the sunspot butterfly diagram. Such a method, dubbed genetic forward modeling, has already been used successfully to infer the rotational profile of the deep solar core from low-ℓ rotational frequency splittings (see Charbonneau et al. 1998).

Genetic forward modeling could also be used to invert stability diagrams for the emergence of BMRs. Our best-fit emergence function has $a = 0$ in Equation (10), implying that the emergence probability is primarily set by the strength of the toroidal magnetic component, in agreement with the idea that sunspots form from axisymmetric toroidal magnetic flux ropes located at or near the base of the convection zone. However, our eruption threshold of $\simeq$200 G is rather low, even if some level of amplification is expected in forming a compact flux rope from a diffuse magnetic field. There is clearly room for improvement in this model component.

6. CONCLUSIONS

In this paper we have described a new solar cycle model based on the BL mechanism of poloidal field regeneration through the surface decay of active regions. This new model is based on the coupling of a conventional latitude–longitude simulation of surface magnetic flux evolution (as described in Paper I), coupled to an equally conventional axisymmetric kinematic FTD model defined in a meridional plane (closely following Charbonneau et al. 2005). The novelty lies in the coupling between these to model components: the surface flux evolution simulation provides the source term of the internal dynamo through the surface boundary condition; while the internal dynamo provides the magnetic flux emergence, in the form of pseudo-sunspot bipolar pairs, that act as a source in the surface magnetic flux simulation. The properties of these synthetic bipolar pairs—flux distribution, component separation, tilt angles, etc.—are tailored to reflect observed statistical properties of real sunspots and active regions, as documented in Paper I (Appendix).

The other key aspect of the coupling is the emergence function, which controls the probability of bipole emergence as a function of the spatiotemporal distribution of the deep-seated magnetic field produced by the dynamo component of the coupled model. The emergence probability is assumed to scale linearly with this emergence function, with the proportionality constant acting as the dynamo number for the full coupled model.

The coupled model involves a number of parameters and functionals that cannot be set from first principles, and thus must be optimized to provide the best possible fit to solar observations. We opted to carry out this optimization task through a genetic algorithm-based maximization of the fit between the spatiotemporal distribution of sunspot emergences (butterfly diagram) as produced by the model, and the cycle 21 emergence data of Wang & Sheeley (1989). This scheme returns not only a globally optimal solution, but also Monte Carlo-like error estimates on best-fit parameters values.

The magnetic cycles generated by this dynamo model are intrinsically non-steady, due primarily to the large statistical scatter about the mean east–west tilt pattern of BMRs (as embodied in Joy's law). This is expected, since the axial dipole component of the bipolar pair is determined by this tilt. As a consequence, a critical dynamo number can only be defined in a statistical sense.

A quenching parametrization of the mean tilt angle based on the strength of the internal magnetic field readily stabilizes the mean cycle amplitude, but large fluctuations about this mean nonetheless persist. Such a quenching is consistent with the modeling of the buoyant rise of thin magnetic flux tubes (see Fan 2009, Section 5.1.2, and references therein) and, at the relatively mild level taking place in our dynamo model, does not conflict with extant observational analyses (see Pevtsov et al. 2014). One consequence of tilt quenching is that a very high-amplitude cycle tends to be followed by a lower-than-average cycle. This alternation would tend to amplify over time were it not for the stabilizing effect of the linear sink term used in Equation (8) with $\tau_R = 10$ years. Very low-amplitude cycles can also be produced by unfavorable emergence patterns, which then lead to persistently low amplitudes in subsequent cycles, with slow recovery to normal amplitude values.

Even though the amplitude of successive simulated cycles are strongly affected by the specific stochastic realization of flux, separation and tilts in the course of a given cycle, even in the linear regime the cycle period is largely insensitive to the value of the dynamo number. The magnetic cycle is also characterized by good hemispheric coupling, in terms of both hemispheric cycle amplitude and timing of hemispheric minima/maxima.

As a descriptive representation of the observed solar cycle, the model reproduces a number of well-known features. The dipole peaks at or slightly before the time of pseudo-sunspot cycle minimum, and its amplitude shows no correlation with the maximum pseudo-SSN of the ending cycle. This is a direct consequence of the strong stochasticity introduced by the realization of tilt patterns throughout the cycle, which is the primary source of cycle amplitude fluctuations. However, the model reproduces the observed positive correlation between dipole strength at cycle minimum and the amplitude of the subsequent pseudo-sunspot cycle. This indicates that, as in the real Sun, the dipole moment generated in the model is a good precursor of cycle amplitude.

Room for improvement certainly remains. The model fails to reproduce the observed moderate anticorrelation between cycle amplitude and duration, yielding instead a very weak positive correlation between these two quantities. While a few extant kinematic FTD models do better in this respect (e.g., Karak & Choudhuri 2011), another possibility is that the origin of this pattern is to be found in dynamical effects, namely the magnetic back-reaction on large-scale flows. The recent analyses of Passos et al. (2012) suggest that an increase in the speed of the deep equatorward meridional flow may indeed be driven by a higher-than-average large-scale magnetic field, which in advection-dominated FTDs would be expected to lead to a proportional reduction in cycle period (see, e.g., Dikpati & Charbonneau 1999).

The long-timescale behavior of the simulated cycles also shows some interesting features, some solar-like and others less so. The model produces a very stable cycle period of 9.5–11 years, but no well-defined low-frequency spectral peaks that could be associated with Gleissberg-like long periodicities. The model does produce occasional Dalton-minimum-like periods of successive low-amplitude cycles, and can also spontaneously shut down the cycle and enter a non-cycling grand-minima-like state, through an unfavorable stochastic pattern of bipolar pseudo-sunspot emergences in the course of a cycle. This is a relatively common occurrence for a simulation using the best-fit parameter values obtained in Section 3: more than one half of simulations initialized with distinct random seeds were found to undergo shutdown at some point during a 100-cycle long time span.

In subsequent papers in this series we will investigate cycle fluctuation patterns in greater detail, and quantify the occurrence statistics of Dalton-like minima. The few such events found so far in our extant simulation runs suggest that entry into these failed minima is rapid, from one cycle to the next, while recovery to average cycle amplitudes is more gradual. We also plan to add a weak turbulent alpha-effect in the convective envelope portion of the domain, and investigate whether this can pull the model out of a shutdown state, as existing simulations have already suggested (e.g., Ossendrijver 2000; Karak & Choudhuri 2013; Hazra et al. 2014b).

Because it includes an explicit, spatially resolved representation of the solar "surface," the 2×2D solar cycle model presented here is ideally suited for providing synthetic data for coronal magnetic field reconstructions, as well as for assimilation of magnetographic data toward solar cycle forecasting. The results presented in this paper indicate that an accurate determination of the tilt angles of individual emerging bipolar sunspot pairs will be a critical element of the latter endeavor.

We wish to thank Yi-Ming Wang and Neil R. Sheeley, Jr. for kindy providing us with their comprehensive database of bipolar emergences for cycle 21 and Roger Ulrich for his compilation of latitudinal flow measurements and error estimates. This research was funded by a graduate research fellowship of the Fonds de Recherche du Québec Nature et Technologies (AL) and the Discovery Grant Program (PC) of the Natural Science and Engineering Research Council of Canada. Calculations were performed on Calcul Québec's computing facilities, a member of Compute Canada consortium.

REFERENCES

Babcock, H. D. 1959, ApJ, 130, 364
Babcock, H. W. 1961, ApJ, 133, 572
Babcock, H. W., & Babcock, H. D. 1955, ApJ, 121, 349
Baumann, I., Schmitt, D., & Schüssler, M. 2006, A&A, 446, 307
Baumann, I., Schmitt, D., Schüssler, M., & Solanki, S. K. 2004, A&A, 426, 1075
Bogdan, T. J., Gilman, P. A., Lerche, I., & Howard, R. 1988, ApJ, 327, 451
Burnett, D. S. 1987, Finite Element Analysis: From Concepts to Applications (Reading, MA: Addison-Wesley)
Caligari, P., Moreno-Insertis, F., & Schussler, M. 1995, ApJ, 441, 886
Cameron, R., & Schüssler, M. 2015, Sci, 347, 1333
Charbonneau, P. 2002, NCAR Tech. Note, NCAR/TN-451+STR (Boulder, CO: National Center for Atmospheric Research), 1
Charbonneau, P. 2007, AdSpR, 39, 1661
Charbonneau, P. 2010, LRSP, 7, 3
Charbonneau, P. 2014, ARA&A, 52, 251
Charbonneau, P., Christensen-Dalsgaard, J., Henning, R., et al. 1999, ApJ, 527, 445
Charbonneau, P., & Knapp, B. 1995, NCAR Tech. Note, NCAR/TN-418+IA (Boulder, CO: National Center for Atmospheric Research), 1
Charbonneau, P., St-Jean, C., & Zacharias, P. 2005, ApJ, 619, 613
Charbonneau, P., Tomczyk, S., Schou, J., & Thompson, M. J. 1998, ApJ, 496, 1015
Choudhuri, A. R., Chatterjee, P., & Jiang, J. 2007, PhRvL, 98, 131103
Choudhuri, A. R., Schüssler, M., & Dikpati, M. 1995, A&A, 303, L29+
D'Silva, S., & Choudhuri, A. R. 1993, A&A, 272, 621
Dasi-Espuig, M., Solanki, S. K., Krivova, N. A., Cameron, R., & Peñuela, T. 2010, A&A, 518, A7
Dikpati, M. 2011, ApJ, 733, 90
Dikpati, M., & Charbonneau, P. 1999, ApJ, 518, 508

Dikpati, M., de Toma, G., & Gilman, P. A. 2006, GeoRL, 33, 5102
Dikpati, M., & Gilman, P. A. 2001, ApJ, 559, 428
Dikpati, M., & Gilman, P. A. 2007, SoPh, 241, 1
Durney, B. R. 1995, SoPh, 160, 213
Fan, Y. 2009, LRSP, 6, 4
Fan, Y., & Fang, F. 2014, ApJ, 789, 35
Ferriz-Mas, A., Schmitt, D., & Schuessler, M. 1994, A&A, 289, 949
Gilman, P. A., & Miesch, M. S. 2004, ApJ, 611, 568
Hale, G. E., Ellerman, F., Nicholson, S. B., & Joy, A. H. 1919, ApJ, 49, 153
Hazra, G., Karak, B. B., & Choudhuri, A. R. 2014a, ApJ, 782, 93
Hazra, S., Passos, D., & Nandy, D. 2014b, ApJ, 789, 5
Howard, R. F. 1991, SoPh, 136, 251
Jiang, J., Cameron, R. H., Schmitt, D., & Işık, E. 2013, A&A, 553, A128
Jouve, L., & Brun, A. S. 2007, A&A, 474, 239
Karak, B. B., & Choudhuri, A. R. 2011, MNRAS, 410, 1503
Karak, B. B., & Choudhuri, A. R. 2013, RAA, 13, 1339
Karak, B. B., Jiang, J., Miesch, M. S., Charbonneau, P., & Choudhuri, A. R. 2014, SSRv, 186, 561
Leighton, R. B. 1964, ApJ, 140, 1547
Lemerle, A., Charbonneau, P., & Carignan-Dugas, A. 2015, ApJ, 810, 78
McClintock, B. H., & Norton, A. A. 2013, SoPh, 287, 215
Miesch, M. S., & Dikpati, M. 2014, ApJL, 785, L8
Miesch, M. S., & Teweldebirhan, K. 2015, arXiv:1511.03613
Muñoz-Jaramillo, A., Dasi-Espuig, M., Balmaceda, L. A., & DeLuca, E. E. 2013, ApJL, 767, L25
Muñoz-Jaramillo, A., Nandy, D., Martens, P. C. H., & Yeates, A. R. 2010, ApJL, 720, L20
Nandy, D., & Choudhuri, A. R. 2001, ApJ, 551, 576
Nandy, D., & Choudhuri, A. R. 2002, Sci, 296, 1671
Nelson, N. J., Brown, B. P., Brun, A. S., Miesch, M. S., & Toomre, J. 2013, ApJ, 762, 73
Nelson, N. J., Brown, B. P., Sacha Brun, A., Miesch, M. S., & Toomre, J. 2014, SoPh, 289, 441
Ossendrijver, M. A. J. H. 2000, A&A, 359, 1205
Parker, E. N. 1955, ApJ, 122, 293
Passos, D., & Charbonneau, P. 2014, A&A, 568, A113
Passos, D., Charbonneau, P., & Beaudoin, P. 2012, SoPh, 279, 1
Passos, D., Nandy, D., Hazra, S., & Lopes, I. 2014, A&A, 563, A18
Pevtsov, A. A., Berger, M. A., Nindos, A., Norton, A. A., & van Driel-Gesztelyi, L. 2014, SSRv, 186, 285
Schad, A., Timmer, J., & Roth, M. 2013, ApJL, 778, L38
Schmitt, D. 1987, A&A, 174, 281
Schrijver, C. J., De Rosa, M. L., & Title, A. M. 2002, ApJ, 577, 1006
Schüssler, M., Caligari, P., Ferriz-Mas, A., & Moreno-Insertis, F. 1994, A&A, 281, L69
Snodgrass, H. B. 1983, ApJ, 270, 288
Stenflo, J. O., & Kosovichev, A. G. 2012, ApJ, 745, 129
Ulrich, R. K. 2010, ApJ, 725, 658
van Ballegooijen, A. A., & Choudhuri, A. R. 1988, ApJ, 333, 965
Wang, Y.-M., Lean, J., & Sheeley, N. R., Jr. 2002a, ApJL, 577, L53
Wang, Y.-M., Nash, A. G., & Sheeley, N. R., Jr. 1989, Sci, 245, 712
Wang, Y.-M., & Sheeley, N. R., Jr. 1989, SoPh, 124, 81
Wang, Y.-M., & Sheeley, N. R., Jr. 1991, ApJ, 375, 761
Wang, Y.-M., Sheeley, N. R., Jr., & Lean, J. 2002b, ApJ, 580, 1188
Weber, M. A., Fan, Y., & Miesch, M. S. 2011, ApJ, 741, 11
Yeates, A. R., & Muñoz-Jaramillo, A. 2013, MNRAS, 436, 3366
Zhao, J., Bogart, R. S., Kosovichev, A. G., Duvall, T. L., Jr., & Hartlep, T. 2013, ApJL, 774, L29